

X-ray diffraction (XRD) techniques for materials characterization

4

J. Epp

Foundation Institute of Materials Science, Bremen, Germany

4.1 Introduction

The discovery of X-rays by Wilhelm Conrad Roentgen in 1895 allowed important innovations in all scientific disciplines, making the development of new medical and technical applications possible (Roentgen, 1895). In particular, the research on X-ray diffraction (XRD) by crystals initiated by Laue, Friedrich, and Knipping in 1912 opened new possibilities in the study of crystalline materials (Friedrich et al., 1913). Since then, these methods have been further developed to become very powerful tools in the fields of materials science and engineering. The experimental methods based on X-ray that are used in materials science and engineering can be divided into three main categories (Spieß et al., 2009). X-ray fluorescence spectroscopy is widely used for qualitative and quantitative chemical analysis, in particular, in electron microscopes. The X-ray radiography is an imaging technique based on the registration of the intensity passing through an object by using films or detectors which allow making its internal structure visible due to the local variation of the absorption. One of the major developments of the last decades in this field is the X-ray computer tomography. Finally, the XRD methods are based on the ability of crystals to diffract X-rays in a characteristic manner allowing a precise study of the structure of crystalline phases. Recorded diffraction patterns contain additive contributions of several micro- and macrostructural features of a sample. With the peak position, lattice parameters, space group, chemical composition, macrostresses, or qualitative phase analysis can be investigated. Based on the peak intensity, information about crystal structure (atomic positions, temperature factor, or occupancy) as well as texture and quantitative phase analyses can be obtained. Finally, the peak shape gives information about sample broadening contributions (microstrains and crystallite size) (Dinnebier and Billinge, 2008).

In the field of materials science and engineering, several applications were developed to become state of the art techniques, in particular qualitative and quantitative phase analyses, investigations of crystallographic textures, and residual stress measurements.

The present chapter first presents a condensed overview of the generation of X-rays as well as the theory of diffraction of X-rays by crystals. Afterward, a short survey of the hardware for XRD measurements is given. The methods of phase analysis, residual stress measurements, and texture investigations of polycrystalline materials are then described with practical examples, and finally, special methods and future trends are presented.

4.2 Principles of X-ray diffraction techniques

4.2.1 Generation of X-ray radiation

X-rays are high-energy electromagnetic waves with a wavelength between 10^{-3} and 10^1 nm (Spieß et al., 2009). The generation of X-rays is generally achieved by the use of sealed tubes, rotating anodes or synchrotron radiation sources. Sealed tubes and rotating anodes, which are used in laboratory equipment, both produce X-rays by the same principle. Electrons generated by heating a tungsten filament in a vacuum are accelerated through a high potential field and then directed to a target which then emits X-rays. The incident electrons induce two effects leading to the generation of X-rays: the first is the deceleration of the electrons leading to the emission of X-ray photons with a broad continuous distribution of wavelength, also called *Bremsstrahlung* (Schwartz and Cohen, 1987). The second is the ionization of the impinging atoms by ejecting electrons from the inner shells. In order to get a more stable state, electrons from outer shells “jump” into these gaps. The difference between the electron energies of the inner shell and of the incoming electron is emitted in the form of photons, with a characteristic energy depending on the initial and final shell position of the electrons and on the material as shown exemplarily in Fig. 4.1 (Schwartz and Cohen, 1987). The characteristic radiation requires minimum excitation potential of the electrons to be emitted, which depends on the target material.

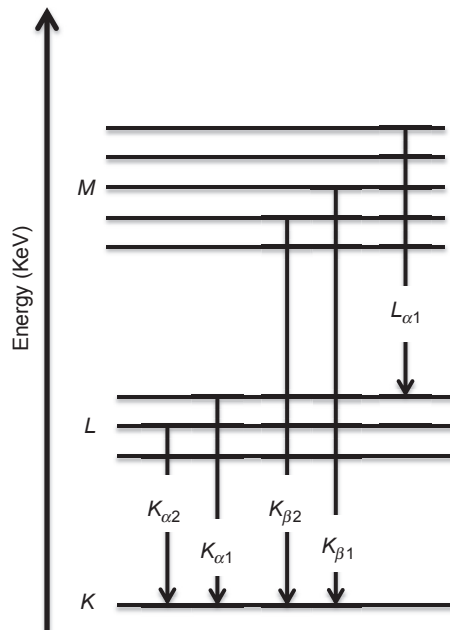


Figure 4.1 Schematic of the atomic energy levels and emission of characteristic X-ray radiation.

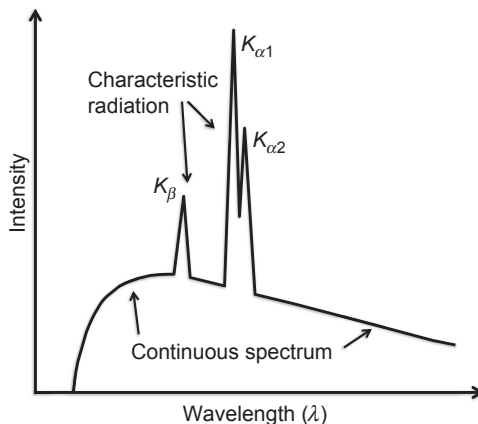


Figure 4.2 Intensity over wavelength distribution of the X-ray radiation produced by a sealed-tube showing the continuous and the characteristic spectrum.

The radiation coming out of a sealed tube or a rotating anode is therefore a superimposition of a continuous spectrum and of characteristic radiations as presented schematically in Fig. 4.2. In general, XRD methods only use the characteristic radiation with the highest intensity, the K_α radiation, and remove most of the remaining radiation by using appropriate filters or monochromators. The filtering is based on the nonlinear absorption of the filter material regarding the wavelength, leading to absorption edges. According to the filter material, the absorption edge is situated at a different wavelength allowing a strong absorption of the continuous spectrum as well as of the K_β radiation while letting most of the K_α intensity passing through. There are appropriate filter materials for all targets. A list of the common target materials with the wavelength of their characteristic radiations K_α and K_β , together with the minimum excitation potential and the required filters is given in Table 4.1.

The production of X-ray radiation in synchrotrons is based on a different principle and is generated by bunches of electrons or positrons which circulate at relativistic energies close to the speed of light. High energy electrons are produced by a high power electron gun and injected in a booster ring for acceleration. The electrons are then introduced in a storage ring where the synchrotron radiation is produced. Modern synchrotron storage rings are generally not circular but have a polygon shape where the electron beam is guided from a straight section to another by dipole magnets (Fitzpatrick and Lodini, 2003). The generation of the radiation takes place in the straight regions where so-called insertion devices are placed. In third generation synchrotrons, wigglers or undulators are generally used, which consist of a periodic arrangement of magnets. The electrons are then forced to follow a sinusoidal path in the orbital plane of the ring leading to the emission of photons. The energy of the emitted photons covers a full spectrum from the infrared to γ -rays (Fitzpatrick and Lodini, 2003). The radiation produced by synchrotron emission has several advantages compared to the conventional method to produce X-rays. First of all, the energy of the radiation can be selected in a wide range that allows the use of the most appropriate radiation for each specific

Table 4.1 List of several common target materials and corresponding wavelength of K_α and K_β radiation in nm together with the minimum excitation potential in kV and the appropriate filter material (Hölzer et al., 1997; Prince, 2004)

Target	$K_{\alpha 1}$	$K_{\alpha 2}$	$K_{\alpha \text{ mean}}$	K_β	Excitation potential	Filter
Cr	0.22897263	0.22936513	0.22910346	0.20848881	5.98	V
Mn	0.21018543	0.21058223	0.21031770	0.19102164	6.54	Cr
Fe	0.19360413	0.19399733	0.19373520	0.17566055	7.11	Mn
Co	0.17889961	0.17928351	0.17902758	0.16208263	7.71	Fe
Ni	0.16579301	0.16617561	0.16592054	0.15001523	8.33	Co
Cu	0.15405929	0.15444274	0.15418711	0.13922346	8.98	Ni
Mo	0.07093000	0.07135900	0.07107300	0.06322880	20.0	Zr

problem. The high energy range (up to 500 keV or more) permits to measure through samples of several mm or cm in thickness. The most important advantage of the synchrotron radiation is the very high brilliance of the generated beam. Therefore, synchrotron radiation is particularly indicated for short measurements of high quality as needed for in situ investigations. However, it requires the application for beam time at one of the synchrotron radiation facilities available over the world, and therefore only a few preselected measurements can be performed in each experiment.

4.2.2 Diffraction of X-ray by crystalline materials

When X-ray photons reach matter, several types of interactions can take place leading to different absorption and scattering effects, which will not be treated here. An elastic (coherent) scattering, also called Rayleigh scattering, occurs between the photons and the electrons surrounding the atomic nuclei. In this case, the energy of the scattered wave is unchanged and it retains its phase relationship to the incident wave (Dinnebie and Billinge, 2008). As a consequence, the X-ray photons impinging on all atoms of an irradiated volume are scattered in all directions (Noyan and Cohen, 1987). However, due to the periodic nature of a crystalline structure, constructive or destructive scattered radiation will result, leading to characteristic diffraction phenomena which can be studied to investigate the crystal structure of materials.

The principle of the methods is based on the diffraction of X-rays by periodic atomic planes and the angle or energy-resolved detection of the diffracted signal. The geometrical interpretation of the XRD phenomenon (constructive interferences) has been given by W.L. Bragg (Bragg, 1913). Fig. 4.3 gives the details about the geometrical condition for diffraction and the determination of Bragg's law. Bragg's law is given in Eq. [4.1].

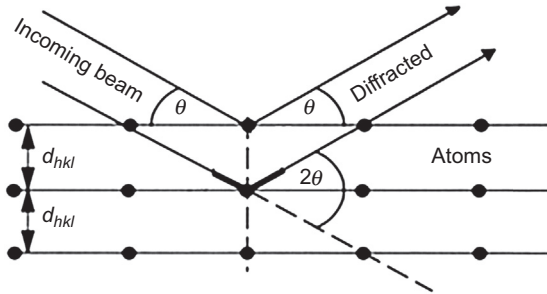


Figure 4.3 Geometrical condition for diffraction from lattice planes (Spieß et al., 2009).

$$n\lambda = 2d_{hkl} \sin(\theta) \quad [4.1]$$

In Eq. [4.1], n is the order of diffraction, λ the wavelength of the incident beam in nm, d_{hkl} the lattice spacing in nm and θ the angle of the diffracted beam in degree. In a polycrystalline, untextured material with fine grains, diffraction occurs for each lattice plane and direction that satisfies the Bragg's law in the case of constructive interferences. This results in the occurrence of diffraction cones appearing in the form of so-called Debye rings or diffraction rings if detected by a plane detector (Fig. 4.4).

The total intensity diffracted by a considered unit cell is described by the summation of the intensity scattered from the individual atoms (Noyan and Cohen, 1987). The diffracted intensities $I_{(hkl)}$ are directly proportional to the square of the crystallographic structure factor $F_{(hkl)}$, which is a complex quantity (Eq. [4.2]) (Will, 2006).

$$F_{(hkl)} = \sum_{j=1}^N f_j \times \exp(2\pi i(hx_j + ky_j + lz_j)) \quad [4.2]$$

with f_j the form factor or atomic scattering factor of atom j , hkl the Miller indices of the diffracting planes and xyz the relative atomic positions in the unit cell. The summation j runs over all atoms in one unit cell (Will, 2006).

According to the crystal symmetry, different extinctions of interferences will occur, leading to different diffraction patterns. For example, in the case of body-centered lattices, diffraction occurs if the condition $h + k + l = 2n$ is satisfied,

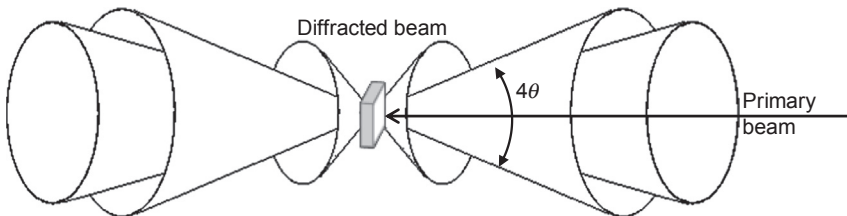


Figure 4.4 Diffraction cones in transmission and reflection occurring for a polycrystalline material.

while in face-centered lattices, the condition $h + k, k + l, h + l = 2n$ has to be satisfied (Spieß et al., 2009).

The total diffracted intensity for a lattice plan family ($I_{(hkl)}$) depends on several factors. These terms are combined to obtain an expression describing the total intensity at any 2θ position (Eq. [4.3]).

$$I_{(hkl)} = K \times \left| F_{(hkl)} \right|^2 \times f_a e^{\frac{-B \cdot \sin^2(\theta)}{\lambda^2}} \times A \times L(\theta) \times P(\theta) \times m \quad [4.3]$$

With K , a constant independent of 2θ , $f_a e^{\frac{-B \cdot \sin^2(\theta)}{\lambda^2}}$ the temperature factor describing the average displacement of atoms from their mean position due to temperature, A the absorption factor, $L(\theta)$ the Lorentz factor which is equal to $1/\sin(2\theta)$, $P(\theta)$ the polarization factor which is equal to $(1 + \cos^2(2\theta))/2$ and m the multiplicity describing the number of equivalent planes that can diffract at a given Bragg angle (Spieß et al., 2009; Noyan and Cohen, 1987).

As real materials always contain imperfections, the intensity distribution of the signal diffracted by considered family of hkl planes can be altered. The shape of the diffracted signal is influenced by different factors, and the resulting signal is then a convolution of the following contributions (Guinebretière, 2006):

- The instrumental broadening which depends on the X-ray source, primary and secondary optics, detector, etc.;
- Composition heterogeneity within the analyzed crystallites (leading to a distribution of lattice constants and so to a possible broadening);
- The size of the coherently diffracting domains (also called crystallite size);
- Crystal defects like dislocations, stacking faults, twins, etc.;
- Inhomogeneous strains and microstrains.

In general, diffraction data are represented as intensity distribution as a function of the 2θ angle. The information content that can be extracted is represented in Fig. 4.5.

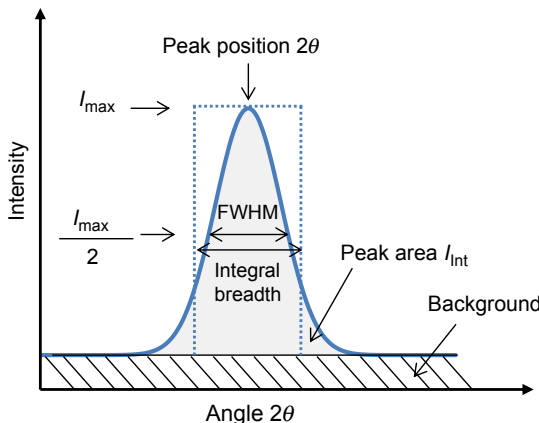


Figure 4.5 Diffraction peak and information content that can be extracted.

After background subtraction, the maximum peak intensity I_{\max} can be defined as well as the integrated intensity I_{int} (area under the peak). The peak position can be determined by several methods (center of gravity, fit of different mathematical function, etc.). The peak width can be generally characterized either by the full width at half maximum (FWHM) corresponding to the peak breadth at half of the maximum intensity, or by the integral breadth (IB), which corresponds to the width of a rectangle of the same maximal and integrated intensity as the considered peak. Depending on the purpose of the measurements, the different peak parameters are used.

As a consequence of absorption and scattering effects, X-rays are weakened along their path in the material. The intensity loss is exponential and follows the general law of Beer–Lambert. The transmitted intensity I can be calculated by Eq. [4.4] with I_0 being the initial beam intensity, x is the thickness of the absorbing layer, and μ is the mass absorption coefficient depending on the wavelength of the X-rays and on the material (Klug and Alexander, 1974). The depth penetration of X-rays produced in laboratory equipment is typically in the range of a few micrometers to a maximum of several tens of micrometers for common wavelengths in metals (Spieß et al., 2009).

$$I = I_0 \times \exp(-\mu \times x) \quad [4.4]$$

4.2.3 Special methods

4.2.3.1 Energy-dispersive X-ray diffraction

The methods presented previously in this chapter are all for the commonly used angle-dispersive measurements, meaning that a (quasi)-monochromatic beam is used while the angular position of the diffraction peaks is measured. An alternative method called energy-dispersive consists of the use of a white beam (polychromatic beam over the complete available wavelength range) and the detection of diffraction peaks at a fixed 2θ angle by using energy-resolved detectors. In this case, the Bragg's law has to be modified as given in Eq. [4.5] (Spieß et al., 2009).

$$E_{hkl} = n \times \frac{h \times c}{2 \times \sin(\theta)} \times \frac{1}{d_{hkl}} \quad [4.5]$$

This method has been mainly developed in synchrotron applications as high beam intensity over a large range of energy is available. One advantage of the method is that no detector movement is needed to record a large number of peaks. As a consequence, rapid measurements can be performed, for example, for in situ analysis. A second advantage is based on the varying penetration depth of the signal due to the covered energy range in the case of measurements in reflexion mode. Thanks to this property, the varying diffraction peaks at different energy levels can be assigned to different depth positions, and therefore analysis of depth profile can be performed without material removal and without sample or detector movement. One main application is the depth-resolved residual stress analysis (Spieß et al., 2009).

4.2.3.2 *Small angle scattering*

The method small angle X-ray scattering allows the investigation of periodic structures within a considered material. In general, measurements are performed in transmission with a monochromatic fine-focused beam at thin samples. The considered range of diffraction angles is thereby smaller than 10° . The principle is still based on the measurement of a diffracted beam by using a 2-D detector. However lattice plans are not considered for diffracting the X-ray beam, but rather, small periodic structures within a material like precipitates, fibers, etc. The phenomenon of diffraction takes place due to variations of electron density at the boundaries of investigated structures. Information about structures with dimensions between 5 and 150 nm can typically be collected. Specific applications can even go to larger structure sizes.

4.2.3.3 *In situ X-ray diffraction*

One major field of special application of the XRD methods is for the investigation of processes under nonambient and temporally changing conditions. These in situ XRD methods were developed over several decades as they present many advantages compared to other techniques like resistivity measurements or dilatometry. In particular, in situ XRD allows to investigate phase-specific properties like lattice parameters, strains, orientations, phase contents, etc., in a direct manner. Sample environments can be as varied as needed for the investigations, such as high pressures and more generally mechanical loading, temperature variations in high temperature ranges, or below room temperature, etc. However, one major barrier for these investigations is the time resolution. With the rapid progress of microelectronics and computers, the methods of in situ XRD investigations could be developed to become more and more accurate with high time resolutions. In particular, the construction of third-generation synchrotrons opened new possibilities in studying very fast processes with time resolutions up to 30 Hz or higher (Curfs, 2002).

In the area of steel research, several phenomena occurring during heat treatment were investigated using standard angle-dispersive methods with synchrotron radiation, like lattice parameter fluctuations in austenite and transformation to bainite (Babu et al., 2007) or phase transformations during welding (Elmer et al., 1996). In situ measurements during mechanical loading were used for the investigation of austenite stability in TRIP-steel (Kruijver et al., 2002).

As already explained in Section 4.2.3.1, methods based on energy-dispersive measurements are also available, allowing recording of energy-dispersive signals from white X-ray beams without any need of detector displacement. Time and depth-resolved texture, residual stress, and phase transformation investigations of rapid processes can be performed, such as the martensitic transformation of filler material for welding (Kromm et al., 2010) or the generation of residual stresses during laser hardening with a measuring frequency of 10 Hz (Kostov et al., 2012).

However, it is not always possible to perform every experiment at a synchrotron as generally only several days of beam time per year are accorded to each project. Therefore, methods of in situ XRD with laboratory equipment are also of great interest. Due to much lower signal intensity and energy, the methods of laboratory in situ

XRD are much more difficult to apply than at synchrotron. Major problems include time resolution and undesired surface modification during heat or surface treatment as the depth penetration of laboratory X-ray is low (Recke and Hirsch, 2007). Several processes could already be investigated, such as thermal residual stress relaxation of steels coated by chemical vapour deposition (CVD) by using a position sensitive detector (Tomala, 1998) or the formation of nitride layers and the generated stresses during gas nitriding treatment (Günther, 2004). Finally, phase transformations and carbide dissolution kinetics during isothermal holding and continuous heating (Epp et al., 2007) as well as the martensitic transformation during rapid quenching (Rocha et al., 2005) could be recently investigated thanks to a 2-D detector and rotating anode, allowing faster measurements.

4.2.4 Hardware for X-ray diffraction measurements with laboratory equipment

Modern lab diffractometers are computer-controlled and equipped with different hardware depending on their scope of action. The instruments are all composed of an X-ray source, primary and secondary optics, a goniometer, a sample holder, and a detector. Generally, stationary equipment is used in labs. However, in particular in engineering applications, the investigation of very large or heavy components can be required, and therefore mobile X-ray diffractometer, which can be directly placed on the part to investigate, is available. Such equipment will, however, not be treated in the present section.

4.2.4.1 X-ray source

The different possibilities for the production of X-ray radiation and the commonly used wavelength in laboratory equipment were already presented in Section 4.2. The two main aspects of the X-ray production are the intensity of the radiation and the size/shape of the beam coming out of the anode according to the purpose of the measurements. For the generation of X-ray photons, a high-voltage acceleration of electrons coming out of a tungsten filament is necessary. Generally acceleration voltage between 20 and 60 kV are used. As 99% of the energy used for the production of X-ray is dissipated in heat and only 1% is available for the generation of the radiation, heat development is a major issue limiting the brilliance of the X-ray beam (Spieß et al., 2009). Continuous water cooling of the anode is therefore mandatory, and only low current below 60 mA can generally be used in standard X-ray tubes, limiting the beam intensity. Higher current and consequently higher beam intensity can be achieved by using rotating anodes, as the point of the electron impingement is continuously changed at high speed (up to 25,000 rpm) and therefore the local heat development can be limited.

Common X-ray tubes and rotating anodes allow the use of two types of focus shape depending on the outlet window which is used (sealed tubes generally have four outlet windows, one at each side of the tube: two with point and two with line focus). For texture, residual stress measurements and phase analyses with high spatial resolution

point focus should be chosen, while line focus can be used for phase analysis or residual stress measurements when a large area can be measured as much higher signal intensities are achievable, due to larger irradiated area on the sample.

In the last decades, microfocus tubes using air cooling were developed, allowing very small focus size and high beam intensity. These are particularly indicated for measurements with very high spatial resolution (\varnothing from 10 to 200 μm).

4.2.4.2 Goniometer

All laboratory equipment is equipped with a goniometer, which is the central part of the diffractometer allowing to move the X-ray source, the sample and the detector relative to each other in a very precise manner. In general, Bragg–Brentano geometry is used, which means that the distance between the sample and the detector is constant for all θ angles. For the investigation of powder or massive samples with laboratory equipment, the reflexion mode is generally used as the strong absorption of the X-ray beam by the material does not allow transmission measurements. Two major basic types of goniometer are widespread: θ/θ goniometers, where the sample is fixed (Fig. 4.6(a)), while the X-ray source as well as the detector moves, and $\theta/2\theta$ goniometers for which the X-ray source is at a fixed position while the sample and the detector are moving (Fig. 4.6(b)).

For residual stress and texture measurements, additional rotation axes are generally required in order to position the sample as needed for these investigations. The in-plane rotation of a sample (azimuth angle φ) and the tilt-angle (also called pole angle χ) are commonly available (so-called four-circles goniometers). The χ -rotation can be either achieved by eulerian cradle, as shown in Fig. 4.7, by special tilting devices or by using a robot arm.

According to the sample geometry and the purpose of the measurement, specific sample holders (eg. to achieve automatic sample positioning, automatic sample changing, continuous sample rotation or translation, etc.), or even a controlled sample environment for in situ investigations can be used. In the case of powder samples, amorphous polymer or glass plates can be used to carry the powder. For solid samples, in particular

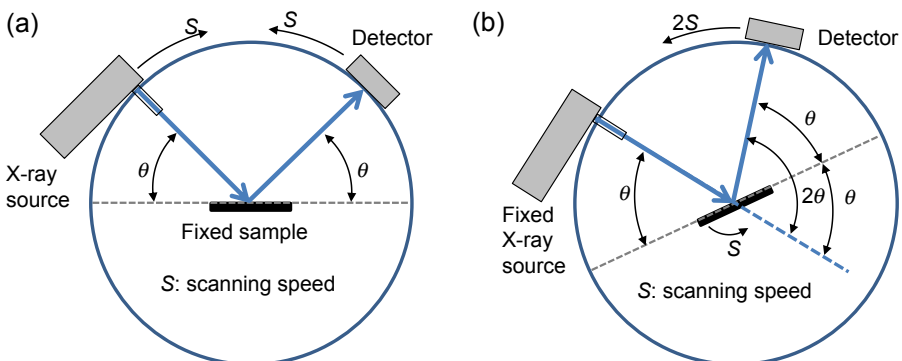


Figure 4.6 Principle of (a) θ/θ goniometers and (b) of $\theta/2\theta$ goniometers.

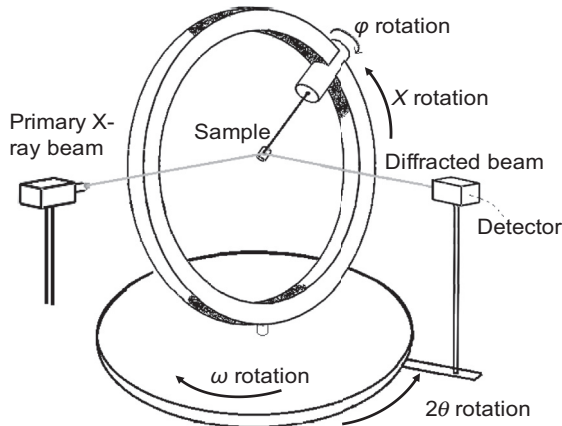


Figure 4.7 Principle of a four-circles goniometer.

for engineering applications, heavy samples and complex geometries are common. Therefore, adapted sample positioning devices have to be used.

4.2.4.3 Primary optics

In order to define the size and form of the primary beam as well as to obtain the highest possible signal intensity or to select the wavelength precisely, special optical devices can be used.

With the use of single crystal monochromators, a specific wavelength can be defined and a monochromatic beam, generally $K_{\alpha 1}$, can be selected, while $K_{\alpha 2}$ and K_{β} can be removed. Several crystals are available, allowing for the selection of a defined wavelength (see Ref. [Spieß et al., 2009](#)). Monochromators have also been developed to allow a parallelization of the beam. These optics, commonly named Göbel mirrors, are multilayer coated optic systems and consist in a succession of strongly and weakly scattering materials arranged in a defined manner. They are particularly indicated for the investigation of irregularly shaped samples and for applications where high beam intensity or high angular resolution is needed.

In order to define the size and the shape of the divergent X-ray beam coming out of the anode, different optical devices can be employed. In the case of line focus, slit systems comprising antiscattering slits and divergence slits are generally used, allowing reducing the beam size and its divergence. According to the number, the position and the opening of the slits, the beam size reaching the sample can be defined.

Another common type of optics are Soller slits, which are generally composed of 20–40 thin plates of metals with high absorption, piled in parallel with a small gap and with a defined length. Divergent beam parts are absorbed and only parallel or slightly divergent beam parts are coming through the slits. With this type of optic, the size of the beam is not directly modified, but only its divergence. They can be applied to reduce the divergence in vertical or in horizontal direction. As a consequence, the total beam intensity is strongly reduced. This type of optic is indicated for measurements where high angular resolution of the peaks is required.

In the case of point focus sources, pinhole collimators are widely used, in order to define the size of the primary beam and control its divergence by removing a part of the incoming intensity. The opening diameter (\varnothing generally from 0.5 to 3 mm) and the length of the collimator are the main parameters. For applications where small beam size is required ($\varnothing < 0.5$ mm), such collimators are not suitable as only a very small portion of the original beam intensity is available, and therefore only very low signal intensity can be recorded. In such cases, special glass fiber optics are generally used. In monicapillaries, one single glass tube with the desired hole diameter is used, which allows an increase in the outgoing beam intensity by total reflexion of a part of the divergent incoming beam. Polycapillary optics, which use a large number of glass fibers, are more effective. Thanks to these, the original beam diameter can be reduced to very small beam diameters (down to 20 μm) without losing much intensity. According to the purpose of the measurements, parallel or focusing polycapillaries can be used, leading to a parallel or a focused beam.

4.2.4.4 Secondary optics

Secondary optics are devices placed between the sample and the detector and are used to define the diffracted beam. Several components described for the primary optics can also be used as secondary optics. Systems of slits are generally used to reduce the divergence of the beam and lead to narrow peaks but with intensity lost. As well, Soler slits can be used to reduce the beam divergence and achieve higher angular resolution. Secondary monochromators can be used in order to remove undesirable wavelengths such as K_β radiation or fluorescent radiation (for example, in the case of $\text{Cu-}K_\alpha$ radiation used for the investigation of Fe-based material). Filters to reduce the K_β radiation (see [Section 4.2](#)) can generally be placed in front of the detector.

4.2.4.5 Detectors

Several types of detectors are available for the detection of the diffracted beam intensity. The working principle of the detectors is based on the conversion of impinging X-ray photons into another signal which can be analyzed. Several technologies are available for the detectors. Gas detectors are based on the ionization of a gas by the incoming X-ray photons that generate voltage pulses. Solid detectors use the phenomenon of fluorescence of special materials and either convert into voltage pulses or into visible light that can be recorded by a charged coupled device (CCD) camera. Finally, semiconductor technologies are also available for the detection of X-rays. These have a very good energy resolution and are therefore widely used in an energy-dispersive measurement mode ([Guinebretière, 2006](#)).

These detectors can be classified in three categories, according to the size of their active detecting area. Zero-dimensional detectors are point detectors, which means a very small angular range is recorded at one detector position. Point detectors are generally either proportional counters (gas ionization) or scintillation counter (fluorescent crystal). One-dimensional detectors (position sensitive detectors (PSD)) have a large active detecting area in 2θ (from a few $^\circ$ to 120° 2θ) but a limited height

(Guinebretière, 2006). Such detectors are often based on gas ionization in combination with a counter wire allowing the spatial localization of the incoming X-ray photons by analyzing the time delay of the impulses at both ends of the wire (Spieß et al., 2009). Two-dimensional detectors are in form of plane or curved plates that can measure a large part or even complete diffraction rings (Spieß et al., 2009). The working principle of such detectors can be either as PSD by using multiwire techniques or based on CCD camera technologies (Spieß et al., 2009). With the use of 1-D and 2-D detectors, time can be gained because a large angular range can be recorded simultaneously. In the case of 2-D detectors, the large portion of diffraction rings that can be measured can allow analyzing texture or residual stresses from one single measurement and can be very useful in the investigation of materials with very large grains or in microdiffraction, leading to spotty rings (He et al., 2000).

4.3 Applications

4.3.1 Qualitative and quantitative phase analysis

Materials for engineering applications are generally optimized regarding their mechanical properties by controlling the present phases and their distribution. Therefore, complex multiphase materials result. In particular, for the development of new alloys or of new production technologies, but also in the context of failure analysis and identification of the present phases, determination of the respective phase contents are of great importance.

4.3.1.1 Measurement of diffraction patterns by X-ray diffraction

As explained in the previous sections, different lattice planes are in diffracting conditions, and varying intensities of the diffracted signal occur according to the crystal structure and space group of the present phases. As a consequence, each phase produces a characteristic diffraction pattern that allows its identification. Moreover, when several phases are present in a system, the characteristic patterns of all phases are superimposed and the intensity of the diffraction peaks of the phases are respectively proportional to their amounts. Therefore, XRD methods are widely used for the identification of present phases (qualitative analysis) and for the determination of their respective amounts (quantitative analysis).

In order to perform a qualitative/quantitative phase analysis, a diffraction pattern covering a large 2θ range has to be measured in order to record as much diffraction peaks as possible. For this, the different hardware presented in the previous section can be used. Generally, so-called coupled scans are performed, which means that the sample is always at half the position of the detector in the case of a $\theta/2\theta$ goniometer, or that the X-ray tube and the detector are always at the same angle θ in the case of a θ/θ goniometer. In special cases, uncoupled scans can be performed where the θ and 2θ angles are independently moved. One main application of this strategy is the grazing incidence method, where the primary beam is reaching the sample by a constant

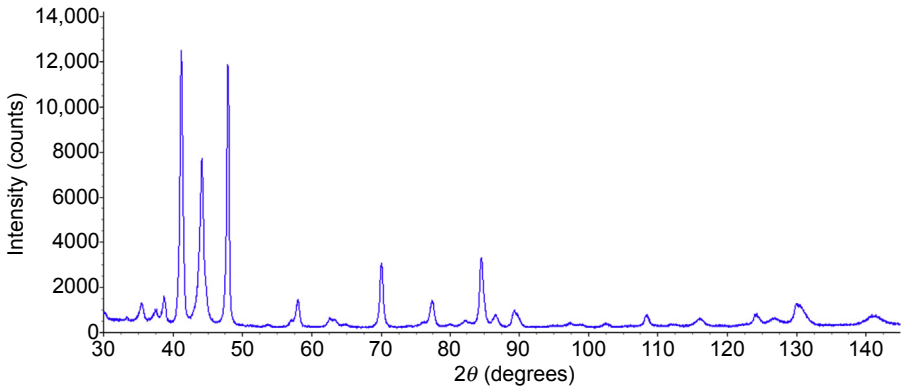


Figure 4.8 Diffraction pattern of a nitrided tool steel X40CrMoV5-1.

and very flat angle (generally between 1° and 5°) while only the detector is scanning. This method is applied for the investigation of thin films in order to reduce the penetration depth of the X-ray beam inside the sample by increasing the beam path.

In order to achieve reliable phase analyses, high quality diffraction patterns are required. Depending on the hardware and on the sample to analyze, the measurement of a diffraction pattern can take between several minutes and 100 h or more. When point detectors are used, continuous scans (continuous scanning of the detector with a defined speed) or step scans (measurements at discrete positions with a defined step size and measurement time for each step) can be performed. In the case of step scans, the step size has to be small enough in order to achieve well-defined peak shapes.

An example of a complex diffraction pattern is shown in Fig. 4.8. The sample is a tool steel of type X40CrMoV5-1 treated by a nitriding treatment leading to the formation of a white layer. The measurement was performed with a $\theta/2\theta$ diffractometer using Cu- K_α radiation with a line focus, divergent slits as primary optics and as secondary optic a Soller slit, a LiF monochromator with a scintillation counter. The measurements were performed in a 2θ range from 30° to 145° with a step size of 0.02° and 20 s/step, leading to a total measurement time of 32 h.

The diffraction pattern contains plenty of peaks over the complete 2θ range, showing varying and partially overlapped intensity. In order to identify the present phases and quantify their respective amounts, the different methods of qualitative and quantitative phase analysis can be employed.

As already remarked in Section 4.2.2, the penetration depth of X-rays is generally limited to a small surface layer of some micrometers. When measurements in deeper layers are required, a material removal is needed. This can be the case, for example, when the very surface of a sample has been modified and is not representative of the bulk material or when depth profile of residual stresses or phase contents is needed. For this, it has to be ensured that the material is not influenced by the layer removal operation. Therefore, local electrochemical etching of the surface is often used, as no mechanical load and no pronounced heat development occur.

4.3.1.2 Qualitative phase analysis

Once a diffraction pattern has been measured, a qualitative phase analysis can be performed. In order to identify the present phases, a comparison of the present diffraction peaks with known data from a database has to be performed. The main available database is provided by the International Center for Diffraction Data (ICDD) and is based on different scientific sources (<http://www.icdd.com/>). According to the special needs of the users, different databases, called powder diffraction files (PDF), can be purchased: PDF-2 for nonorganic materials, PDF-4 for organics, PDF-4 for minerals or PDF-4+, which contains all entries as well as additional information about atomic coordinates of the phases, etc. These databases contain at the present time up to 500,000 entries. For each documented phase, lattice structure, space group, lattice parameters, and the corresponding position, intensity and indexation (Miller's indices) of diffraction peaks are available.

In the past, the data were available as a system of classified cards (joint committee on powder diffraction standards (JCPDS)) which could be consulted and the peak information had to be compared manually in order to identify the present phases. The databases are now available electronically and can be integrated in the software packages of most of the providers of diffraction equipment. Thanks to this, the comparison of the present peaks is computer-assisted so that the identification of present phases is much more convenient.

After the measurement of the diffraction pattern, a data treatment can be required in order to achieve reliable results. In general, the background has to be subtracted from the measured pattern. Further pattern treatment, such as mathematical removal of $K_{\alpha 2}$ radiation or smoothing operations, might be indicated. Depending on the software, the peak search can be performed by different methods: manual marking or automatic identification by intensity threshold, peak shape specification, and first or second derivatives (Spieß et al., 2009).

In order to start phase identification, several input data are required in order to achieve reliable results. First of all, the nature of the analyzed sample has to be known and inputted into the software as inorganic, organic or mineral. Then, the chemical elements which should be taken into account for the possible phases have to be selected. For this the knowledge about the chemical composition of the analyzed sample is required and therefore at least a qualitative element analysis should be available (better to have a quantitative full analysis). All elements which are not present can then be discarded, while available elements can be marked as "mandatory" or as "possibly present" for the considered phases.

The measured peak data are automatically compared with the entries of the database that fulfill the criterion, which results in a list of possible phases. For each phase, quality marks giving information about the quality and the reliability of the data are specified and should be considered in order to evaluate the results. For every proposed phase, theoretical peak positions and the associated theoretical intensity are shown superimposed to the measured pattern. In order to evaluate whether a proposed phase is present or not, several approaches can be used. A list containing the number of matching and of nonmatching peaks is given from the automatic comparison of the present peaks with the

theoretical peaks of a phase from the database. A figure of merit is calculated on this base in order to evaluate globally how good each phase matches, with the smallest value being the best figure. After preselection of possible phases based on this information, a visual (manual) control has to be performed. Deviations from ideal peak positions due to solid solution or strains as well as intensity variations have to be taken into account. In the case of fine powder samples, texture effects as well as macroscopic strains can be avoided, and therefore the theoretical patterns can match the measurements quite well. On the other hand, solid samples and engineering components can exhibit strong textures, large grains (and therefore irregular peak shape due to poor diffraction statistic) or peaks shifts due to high macroscopic strains. The final selection of the present phases can therefore only be performed by the user on the base of the proposed results and of his knowledge about the investigated sample and the measurement conditions. In an ideal case, all measured diffraction peaks should be assigned to a phase.

As an example, the diffraction pattern of a nitrided tool steel previously presented in Fig. 4.8 has been analyzed with the software EVA (Bruker-AXS, Karlsruhe, Germany) including the PDF-2 database. With the knowledge of the chemical composition of the surface layer and of the core, the elements N, O, Cr, and Fe were taken into account for possible phases. Fig. 4.9 present the diffraction patterns with the identified phases. All major peaks were assigned to Fe_3N and Fe_4N nitrides, while small peaks corresponding to CrN were also identified. Due to the thickness of the nitride layer and the penetration depth of the radiation, the α -Fe matrix below the white layer could also be identified. Finally, as a consequence of the formation of a thin oxide layer at the surface, small peaks corresponding to Fe_3O_4 were also identified. For each identified phase, the positions and the intensity of the theoretical peaks are given. Additional

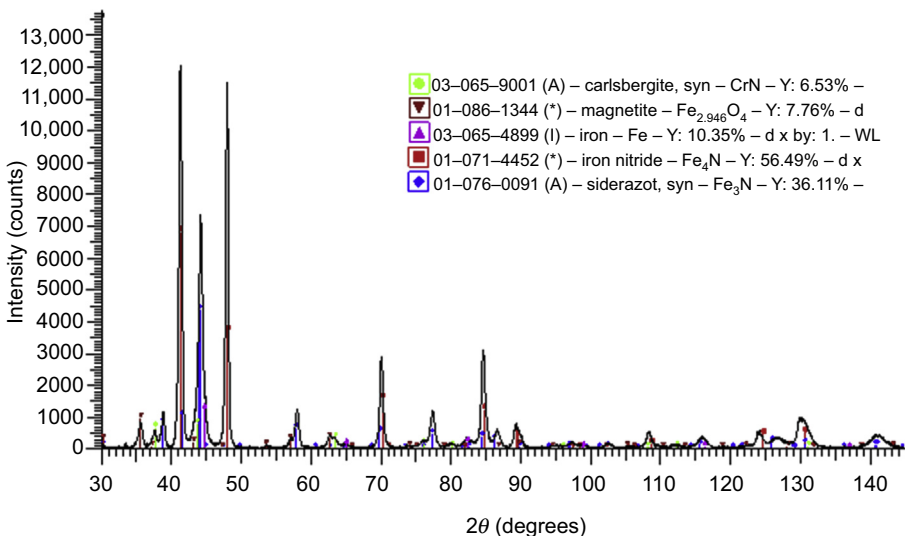


Figure 4.9 Qualitative phase analysis of a nitrided tool steel X40CrMoV5-1.

information like the reference numbers of the identified phases, chemical formula, lattice parameters, etc. are available for the different phases.

4.3.1.3 Quantitative phase analysis

Once the present phases are known, quantitative phase content analysis can be performed. In the case of multiphase compounds, the determination of phase contents can generally not be performed directly on the base of the measured integrated intensities as if the phases have different mass absorption coefficients, the intensity evolution is not linear with the increasing amount (Klug and Alexander, 1974). According to the investigated sample and the purpose of the analysis, different methods can be used:

- Method with external standard
- Method with internal standard
- Method of intensity ratio
- Rietveld method

Method with external standard

The method with external standard consists of comparing the intensity of the reflexion measured at a multiphase material with the intensity of a pure sample of the considered phase measured under the same experimental condition. The volume fraction of the considered phase in the multiphase material (V_i^s) can be calculated by the intensity ratio of the integrated intensity of a given (hkl)-peak of the considered phase within the investigated sample $I_i^s(hkl)$ and of the pure phase $I_i^p(hkl)$, by taking into account the mass absorption coefficients of the pure phase (μ^p) and of the sample (μ^s) as given in Eq. [4.6].

$$\frac{I_i^s(hkl)}{I_i^p(hkl)} = V_i^s \times \frac{\mu^p}{\mu^s} \quad [4.6]$$

One advantage of this method is that it allows determining the amount of amorphous or of not-considered phases. However, it requires the experimental determination of the mass absorption coefficient of the analyzed sample (Spieß et al., 2009).

Method with internal standard

The method with internal standard is well indicated for the analysis of compounds with more than two phases and is based on the addition of a standard phase with defined volume or mass in the investigated compound. This is, of course, only possible for powder samples. As a consequence, the knowledge of the absorption coefficient is not required anymore. The mass concentration of the phase of interest W_i is then proportional to the intensity ratio of considered $I_i(hkl)$ and added phase $I_j(hkl)$ by taking into account a factor K_{ij} and the mass concentration of the added phase W_j (Eq. [4.7]) (Dinnebier and Billinge, 2008).

$$W_i = K_{ij} \times W_j \frac{I_i(hkl)}{I_j(hkl)} \quad [4.7]$$

The factor K_{ij} can be determined experimentally by measurement of known mixtures of the standard and of the considered phase. In order to be able to use this method, it has to be ensured that the peaks of the added standard are not overlapped to other peaks of the compound.

One variation of this method is the reference intensity ratio (RIR) which is based on the intensity ratio with the corundum (113) peak (Dinnebier and Billinge, 2008). One major advantage of this method is that once the required factors have been determined for the phase of interest, no standard phase is longer needed in the compound (Dinnebier and Billinge, 2008).

Method of intensity ratio

The method of intensity ratio consists in calculating directly the intensity ratios of the reflexions of each present phase in a sample by correcting them with factors taking into account multiplicity and other parameters for each reflexion. This method is well indicated for solid samples for which the addition of an internal standard is not possible. Moreover, the knowledge of the absorption coefficient of the phases is not required. In order to calculate the amount of each phase, the total amount of the considered phases has to be known or to be scaled to 1. The calculation of the volume fraction of phase i (V_i) in the measured material can be calculated on the base of the integrated intensity of a peak of this phase $I_i(hkl)$ and of other present phases $I_j(hkl)$ by taking into account phase- and peak-specific factors ($R_x(hkl)$) as given in Eq. [4.8] (Spieß et al., 2009). The factors $R(hkl)$ can be calculated or determined experimentally. With this method, different peak combinations can be used, allowing calculating mean phase content and so possible errors due to texture effects or other factors can be reduced.

$$V_i = \left(\sum_j \frac{I_j(hkl)}{I_i(hkl)} \times \frac{R_i(hkl)}{R_j(hkl)} \right)^{-1} \quad [4.8]$$

One common application of this method is the quantitative analysis of retained austenite and martensite in hardened steel. For this, tables containing R -factors can be found in the literature for the different diffraction peaks of martensite and retained austenite depending on the used wavelength (ASTM, October 2000).

Rietveld method

Contrary to the previous methods, the Rietveld method is a whole pattern method. This means that the evaluation is based on the simultaneous analysis of several peaks. Here, the whole measured pattern is refined with a calculated pattern taking into account several structural, microstructural, and experimental parameters (Will, 2006). The refinement is performed by minimization of the function S given in Eq. [4.9].

$$S = \sum_i u_i |y_{iobs} - y_{icalc}|^2 \quad [4.9]$$

In this equation, y_{iobs} the measured and y_{icalc} the calculated intensities at each 2θ position i and u_i , a weighting factor taken from the experimental error margins, which are assumed to be proportional to the square root of the count rate y_{iobs} following Poisson counting statistics (Will, 2006).

The calculation of y_{icalc} at each position i is a function of instrumental contribution, reflexions of all present phases, backgrounds, etc. All factors depending on each phase of the analyzed sample which are taken into account for the refinement are as follows (Spieß et al., 2009): position of all atoms in the elementary lattice; temperature factor; occupation factor; space group of the lattice; lattice parameters; texture; crystallite size; microstrains; and phase contents. Moreover, several instrumental parameters are also taken into account in order to separate the contribution of instrument and sample. These are: 2θ shifts (error of the instrument); instrumental profile; profile asymmetry; background; wavelength (emission profile); sample positioning error; and absorption (Spieß et al., 2009).

Two distinct strategies are available for profile refinement. The first is based on describing the peak shape by mathematical function such as Gaussian, Lorentzian, Voigt, Pseudo-Voigt, Modified Cox-Hasting Voigt function, Pearson VII, etc. (Will, 2006). These functions can be used for profile refinements if instrumental details are not known. However, these methods are purely based on mathematical fitting and do not allow to extract directly microstructural information from analyzed diffraction patterns, like crystallite size and microstrain. The second strategy available for Rietveld profile refinement is the fundamental parameters approach. With this method, profile calculation is done by convolution of emission profile (W), all instrumental contributions (G) and sample contribution (P), as given in (Eq. [4.10]) (Spieß et al., 2009).

$$Y(2\theta) = (W \otimes G) \otimes P \quad [4.10]$$

All geometrical features of the instrument are described by functions that are convoluted to each other. By correct calculation of the instrumental function, contribution of sample properties to the diffraction pattern can be analyzed (Kern et al., 2004). The instrumental function can also be measured by using a standard without sample broadening. In general, the standard SRM660a (LaB₆) is used, as the large crystallites of about 2 μm do not lead to a significant broadening of the peaks.

At the end of a refinement, it is necessary to check whether the results are reliable and whether they meet certain standard criteria. The overall best criterion for the refinement is difference plots between observed and calculated data. When large discrepancies are present, the different parameters taking into account for the refinement have to be checked. The calculated criterion Residuals weighted profile (Rwp) gives a reliable information about the fit quality. Thereby, the smallest Rwp value represents the best refinement. It is calculated as shown in Eq. [4.11]. The parameter R_{exp} (Eq. [4.12]) represents the minimum expected Rwp depending on the number of

experimental points (N) and the number of refined parameters (Q). The ratio of both parameters gives the goodness of fit (GOF), which can also be used as a criterion of the refinement quality (Eq. [4.13]).

$$R_{wp} = \sqrt{\frac{\sum_i u_i(y_{iobs} - y_{icalc})^2}{\sum_i u_i(y_{iobs})^2}} \quad [4.11]$$

$$R_{exp} = \sqrt{\frac{N - Q}{\sum_i u_i(y_{iobs})^2}} \quad [4.12]$$

$$GOF = (R_{wp}/R_{exp})^2 \quad [4.13]$$

With this method, complex multiphase materials can be analyzed in order to determine the respective phase contents. Also, it can be used for the evaluation of crystallographic texture, crystallite size, strains and microstrains. However, in order to get reliable results, precise information about the crystal structure of the present phases, including the atom coordinates within the lattice, is required.

An example of a quantitative phase analysis by the Rietveld method is shown in Fig. 4.10 for the previously presented nitrided tool steel X40CrMoV5-1. By taking into account the phases identified by qualitative phase analysis, a refinement was performed with the Rietveld-Software TOPAS V4.2 from Bruker-AXS (Bruker-AXS, 2008). A fundamental parameter approach was used after definition of the instrument by measurement of LaB₆ powder.

The refinement is of very good quality so that the measured pattern and the calculated pattern are almost superimposed and cannot be differentiated. The resulting

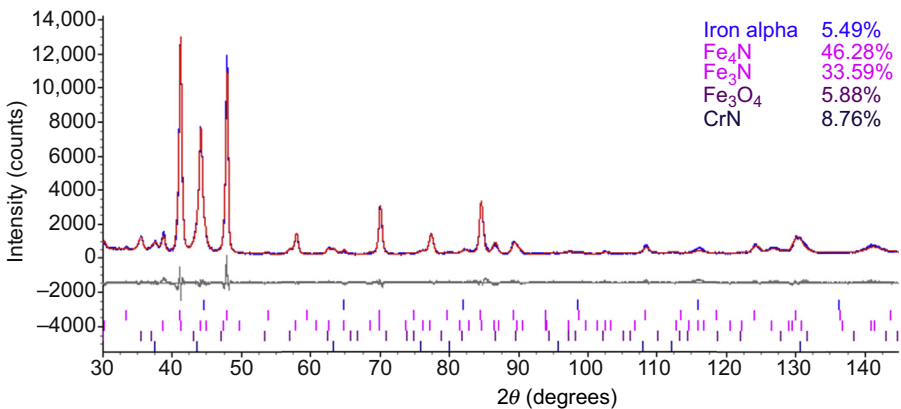


Figure 4.10 Quantitative phase analysis of a nitrided tool steel X40CrMoV5-1 by the Rietveld method.

difference curve is shown over the 2θ angle below the patterns. Only few zones are present where the line is not flat. The Rwp value for this fit is 8.03% while the GOF amounts to 2.01. The result of the quantitative analysis is shown within the diagram for the considered phases: 46.5% Fe_4N , 33.5% Fe_3N , 9.0% CrN , 6.0% Fe_3O_4 , and 5.5% $\alpha\text{-Fe}$. The positions of all diffraction peaks for each phase are shown at the bottom of the pattern.

With this powerful method, very complex multiphase materials can be investigated and quantitative analysis can be performed. However, the method has to be used carefully as many parameters can be refined without physical meaning that would lead to good refinements but erroneous results. Therefore, parameter constraints and control are mandatory for such analyses.

4.3.2 Residual stress analysis

Residual stresses are in general key factors for the later service properties and performance of engineering components. They are, therefore, always more in the focus of research activities as well as of quality management of industrial production. Beside material removal techniques that will not be treated here, XRD is one of the most used methods to characterize residual stresses.

4.3.2.1 Definition of residual stresses

Residual stresses are mechanical stresses which remain at room temperature in a work piece free of any mechanical loading and under homogeneous and temporal stable temperature field. Forces resulting from the residual stresses are balanced over the work piece. Residual stresses are acting forces per unit area (σ^{RS} in N/mm^2 or MPa).

Residual stresses can be classified in three different categories according to their scope of action (Macherauch et al., 1973). Residual stresses of the first kind (σ^I) are the volume average of the position-dependent residual stresses taken over all crystallites and phases within the considered bulk. These represent the macroscopic material balanced over the entire work piece and are also called macroresidual stresses (Eq. [4.14]) (Macherauch et al., 1973). Residual stresses of the second kind (σ^{II}) are deviations from the first-kind residual stresses, for example within grains of different phases (Eq. [4.15]). They are also called homogeneous microstresses (Macherauch et al., 1973). Residual stresses of the third kind (σ^{III}) are local variations at submicroscopic scale, for example due to dislocations or other lattice defects (Eq. [4.16]). They are also called inhomogeneous microstresses (Macherauch et al., 1973). An illustration of the scope of action of the three kinds of residual stresses is given in Fig. 4.11 for a two-phase material composed of α and β grains.

$$\sigma^I = \frac{1}{V_{\text{macro}}} \int_{V_{\text{macro}}} \sigma(x) dV_{\text{macro}} \quad [4.14]$$

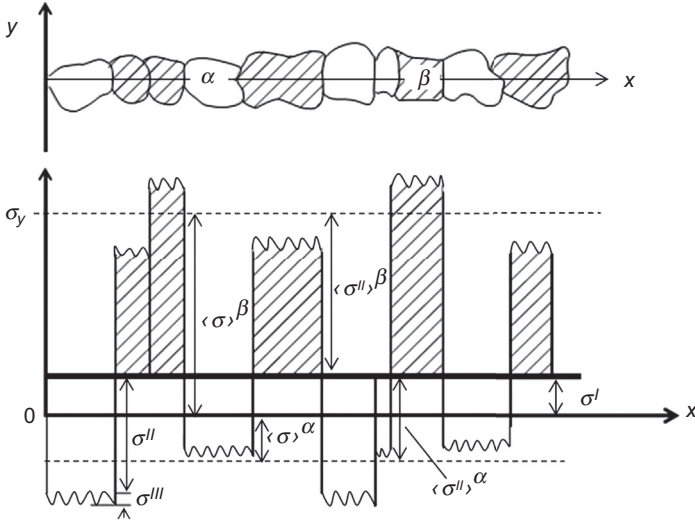


Figure 4.11 Residual stress distribution over several grains of a two-phase material showing the three kinds of residual stresses.

$$\sigma^{II} = \frac{1}{V_{\text{grain}}} \int_{V_{\text{grain}}} \sigma(x) - \sigma^I dV_{\text{grain}} \quad [4.15]$$

$$\sigma^{III}(x) = \sigma(x) - \sigma^I - \sigma^{II} \quad [4.16]$$

In general, the stress state inside a specimen is defined by a symmetric tensor of third order (σ_{ij}) expressed as a function of a coordinate system arbitrarily defined with i the direction of acting force and j the area on which the force is applied (Eq. [4.17]). The stresses acting on planes in orthogonal direction to those are called normal stresses while the stress components acting parallel to the considered planes are called shear stresses.

$$\sigma_{ij} = \begin{pmatrix} \sigma_{11} & \sigma_{12} & \sigma_{13} \\ \sigma_{21} & \sigma_{22} & \sigma_{23} \\ \sigma_{31} & \sigma_{32} & \sigma_{33} \end{pmatrix} \quad [4.17]$$

4.3.2.2 Residual stress measurement

Measurement principle

The methods of XRD for measuring of residual stresses have been well established for more than 30 years (Macherauch et al., 1973). As it is easily accessible, laboratory XRD measurements of residual stress can be applied to a wide range of crystalline

materials. Moreover, this method is phase sensitive, which means that the residual stresses present in different phases of a material can be determined separately, which might be of interest. One of the major aspects of XRD residual stress analysis is that in most cases, no standard or precise reference values are required for the determination of residual stresses.

The method is based on the measurement of the lattice spacing of considered lattice plans (hkl) allowing the determination of strains in a given direction. Fig. 4.12 presents the basic principle of XRD stress measurement showing a stress-free lattice with a lattice spacing d_0^{hkl} leading to a diffraction peak at given 2θ angle. If the material is under stress, the lattice spacing d_i^{hkl} can increase or decrease, which leads to a shift of the recorded peak position. The residual stresses of first and of second kind can be evaluated based on this principle.

In order to perform residual stress measurements by XRD, the sample orientation regarding the coordinate system of the equipment used is of major importance. Therefore, the sample coordinate system (S) and an arbitrary laboratory coordinate system (L) defined by the orientation within the measuring equipment should be considered (Fig. 4.13). The associated polar angle ψ and azimuth angle φ describe the orientation of the sample in the coordinate system.

The strain $\epsilon^{hkl}(\varphi, \psi)$ of defined hkl planes at any φ and ψ angle is defined by Eq. [4.18] with d_0^{hkl} being the strain free lattice spacing and $d^{hkl}(\varphi, \psi)$ the lattice spacing measured at any φ and ψ angle.

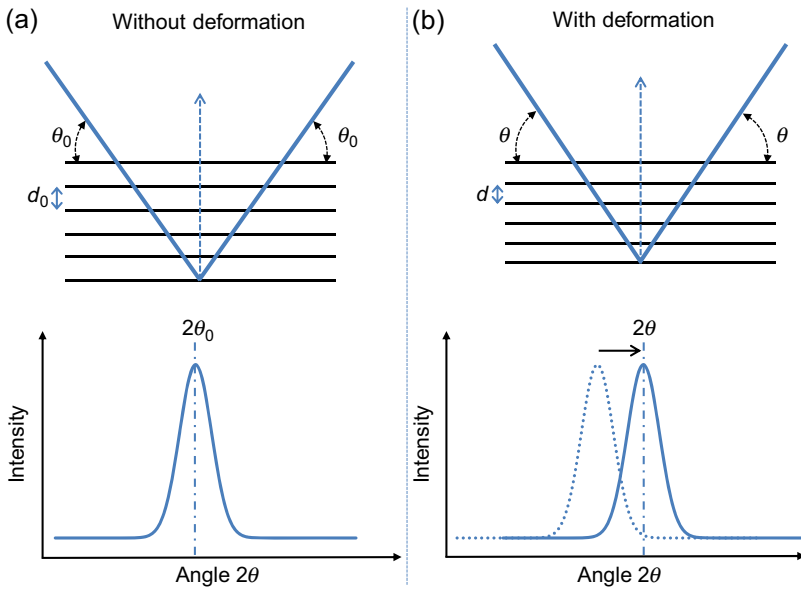


Figure 4.12 Schematic description of diffraction at given hkl planes and corresponding signal recorded by an X-ray diffractometer: (a) for a stress-free lattice; (b) for a lattice under compressive residual stresses.

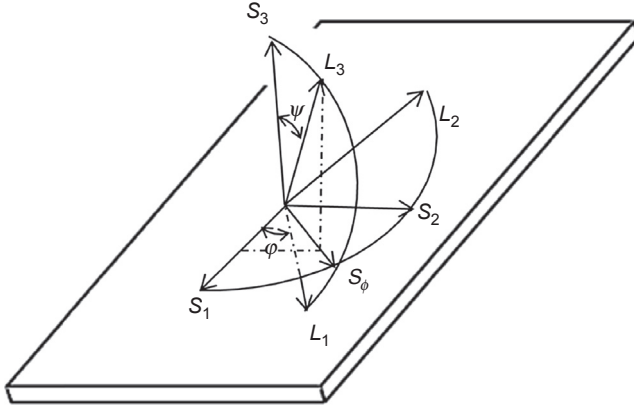


Figure 4.13 Definition of the laboratory coordinate system (L), the sample coordinate system (S) and the associated polar angle ψ and azimuth angle φ (Noyan and Cohen, 1987).

$$\varepsilon^{hkl}(\varphi, \psi) = \frac{d^{hkl}(\varphi, \psi) - d_0^{hkl}}{d_0^{hkl}} \quad [4.18]$$

In order to perform a residual stress measurement by XRD, the evolution of lattice spacing due to the effect of stresses is measured for varying sample orientation. Indeed, when a sample exhibits residual stresses in a given direction, the lattice spacing depends directly on the orientation of the crystallite regarding the present stress. This is illustrated in Fig. 4.14, showing the evolution of lattice spacing $d^{hkl}(\varphi, \psi)$ for different ψ -orientations within a polycrystalline sample exhibiting tensile stresses in longitudinal direction. When the lattice plans are parallel to the considered stress direction (the perpendicular of the lattice plans [the scattering vector] is parallel to the normal to the sample surface; $\psi_1 = 0^\circ$), the lattice spacing is reduced by the Poisson's ratio contraction. When the angle between the scattering vector and the normal to the surface increases, the effect of the present tensile stress on the lattice spacing is continuously increasing. This leads to a continuous growth of $d^{hkl}(\varphi, \psi)$ for increasing ψ value (this behavior is the same when the ψ_i angle is negative). This is also valid for compression stresses where the $d^{hkl}(\varphi, \psi)$ consequently decreases with increasing ψ -angle. When the evolution of the lattice spacing (or of the 2θ angle or of resulting strain) is plotted as a function of $\sin^2\psi$, a linear increase is resulting for simple cases as shown in Fig. 4.15. The slope of the regression line between the measured points is then directly proportional to the present residual stresses by taking into account the elastic properties of the investigated phase for the considered hkl planes. This is the principle of the widely used $\sin^2\psi$ method (Hauk, 1997). Based on this, the measurement of the lattice spacing in at least two different ψ_i angles allows the calculation of the stress. As only elastic strains influences the lattice spacing, only elastic strains leading to stresses can be measured by this method (Prevey, 1986). Also, it has to be mentioned that the residual stress

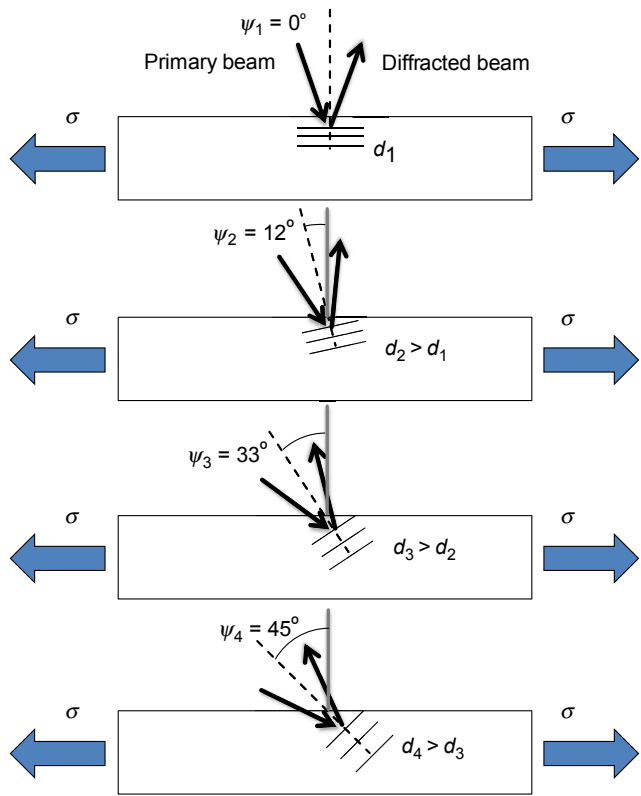


Figure 4.14 Evolution of lattice spacing as a function of the orientation regarding longitudinal tensile stresses.

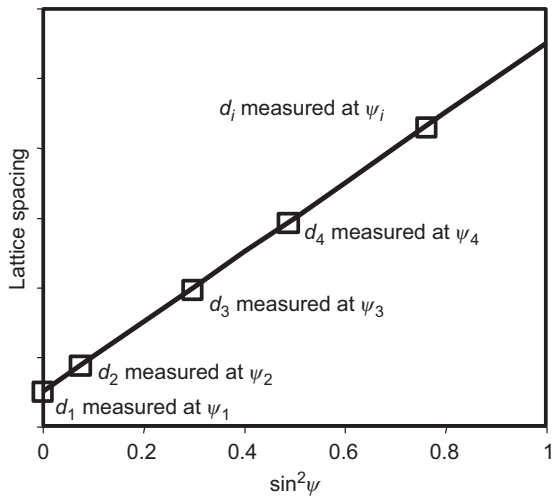


Figure 4.15 Evolution of lattice spacing as a function of $\sin^2 \psi$ for tensile residual stresses.

measured by this principle in a polycrystalline material is an average value of the stress state of thousands of grains of the considered phase within the penetration depth of the X-ray beam.

Depending on the available equipment, the measurements can be performed either in so-called ω -mode or χ -mode. In ω -mode the different ψ -angles are set by a rotation of the sample parallel to the 2θ rotation axis while the angle between the X-ray source and the detector is unchanged. The ψ -angle is then calculated by Eq. [4.19]. In this case, the beam path is asymmetric for all orientations, and depending on the position of the measured peak a strong limitation of possible ψ -angles can result. Moreover, for high ψ -angles, the beam size on the sample can be strongly elongated due to the flat angle of the incoming beam what can lead to problems.

$$\psi = \frac{2\theta}{2} - \omega \quad [4.19]$$

Measurements in χ -mode are performed by tilting the sample out of the plane around a rotation axis perpendicular to the 2θ rotation axis and the ψ -angle is then equal to the χ -angle. This method is well adapted to stress measurement and requires an additional rotation axis for the χ -tilting (eulerian cradle, etc.). The advantage of this method is that the beam path is symmetric for all orientations and that the sample can be tilted to high angles independently on the peak position. Both measurement modes are schematically explained in Fig. 4.16. The angle between the scattering vector (S) (bisector of the incoming and the diffracted beam) and the normal to the sample surface (N) corresponds in both cases to the ψ -angle, used for the calculation of residual stress from the measurements.

In order to determine the complete residual stress tensor, measurements along three different azimuth angles φ (generally 0° , 45° , and 90°) with polar angles (ψ) in negative and in positive direction have to be performed. When principal stress directions are known, measurements can be performed only in one or two azimuth angles.

Data analysis

After recording the diffraction peaks for the different sample orientation, data treatment is required in order to get a reliable determination of peak location. A background subtraction has to be done, and different mathematical correction can be used (Lorentz, Polarization, Absorption, $K_{\alpha 2}$ -removal, smoothing, etc.). After this, the analysis of peak position can be performed by several methods like peak fit using parabola above an intensity threshold or different functions (Pearson VII, Pseudo-Voigt, etc.), center of gravity above one or several intensity thresholds, cross-correlation, etc. (Hauk, 1997).

The strain distribution along any azimuth angle φ and any pole angle ψ is given by following general equation (Eq. [4.20]). The terms σ_{11} , σ_{22} , and σ_{33} represent the normal stresses along three orthogonal directions, and the terms σ_{12} , σ_{13} , and σ_{23} are the shear stresses as given in Eq. [4.17] (Hauk, 1997).

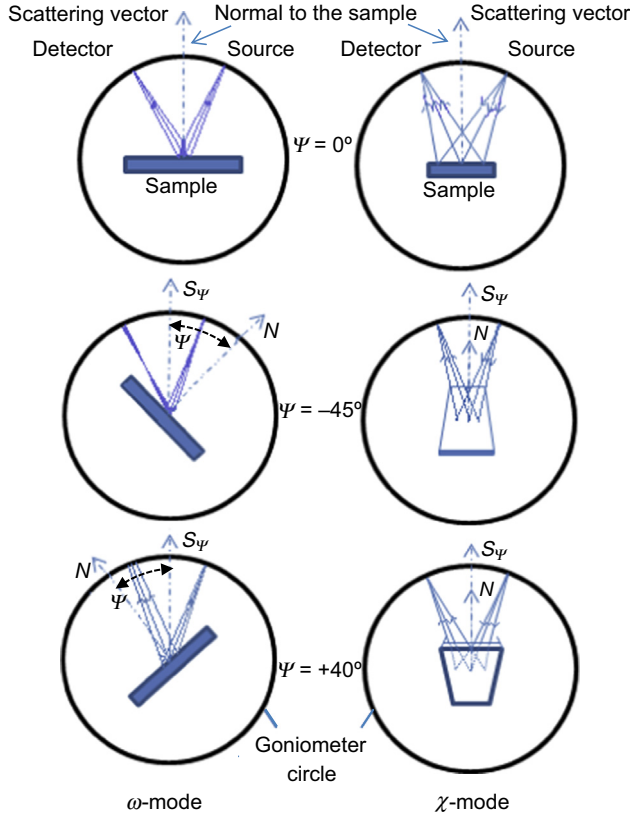


Figure 4.16 Principle of residual stress measurements in ω -mode (left side) and χ -mode (right side) (Macherauch and Zoch, 2014).

$$\begin{aligned}
 \epsilon^{hkl}(\varphi, \psi) = & s_1^{hkl}(\sigma_{11} + \sigma_{22} + \sigma_{33}) + \frac{1}{2}s_2^{hkl}[(\sigma_{11} \cos^2 \varphi + \sigma_{22} \sin^2 \varphi - \sigma_{33}) \sin^2 \psi \\
 & + \sigma_{33}] + \frac{1}{2}s_2^{hkl}[\sigma_{12} \sin 2\varphi \sin^2 \psi + \sigma_{13} \cos \varphi \sin 2\psi \\
 & + \sigma_{23} \sin \varphi \sin 2\psi]
 \end{aligned}
 \tag{4.20}$$

The terms s_1^{hkl} and $1/2s_2^{hkl}$ are the X-ray Elastic Constants and can be calculated from the hkl specific elastic constants as follows: $s_1^{hkl} = -\nu^{hkl}/E^{hkl}$ and $1/2s_2^{hkl} = (1 + \nu^{hkl})/E^{hkl}$, with ν^{hkl} being the Poisson's ratio and E^{hkl} the elastic modulus in MPa of the considered phase for defined hkl planes (Spieß et al., 2009). It has to be kept in mind that even if the investigated polycrystalline material is isotropic regarding its macroscopic elastic properties, the elastic properties of every single grain (or crystallite) are not necessarily isotropic due to crystal anisotropy

and the elastic properties are therefore depending on the investigated lattice planes. Tables containing relevant X-ray elastic constants can be found in the literature (Noyan and Cohen, 1987; Eigenmann and Macherauch, 1995).

In most cases, the term σ_{33} can be considered as being equal to zero, since due to equilibrium conditions, the stresses normal to the surface should be zero within the shallow penetration depth of laboratory X-rays. The $\sin^2\psi$ method can then be used to measure residual stresses in any direction. As it only requires an approximate value of the strain-free lattice spacing, it is a very convenient method. In simple cases, by measuring the lattice spacing along several pole angles ψ at a single azimuth angle φ , the residual stresses are proportional to the slope of the measured lattice spacing over $\sin^2\psi$ and can be determined by following equation (Eq. [4.21]) (Hauk, 1997).

$$\sigma_\varphi = \frac{1}{1/2S_2^{hkl}} \times \frac{\delta d^{hkl}(\varphi, \psi)}{\delta \sin^2\psi} \quad [4.21]$$

However, according to the investigated material, different type of $\sin^2\psi$ curves can be obtained as presented in Fig. 4.17. The first one is the typical linear distribution without shear-stress components σ_{31}/σ_{32} in a normal direction. If such shear-stress components are present, the $\sin^2\psi$ will exhibit a typical ψ -splitting due to asymmetric strain distribution in negative and positive ψ -tilting. In this case, it is mandatory to perform the measurements in both positive and negative ψ -angles to take this into account. Nonlinear $\sin^2\psi$ distribution can occur when residual stress gradients are present within the penetration depth of the X-ray beam or when plastic deformation occurred. The last typical type of $\sin^2\psi$ curve exhibits an oscillating distribution indicating the presence of inhomogeneous residual stress state in the different direction, generally as a consequence of crystallographic texture. For these last two cases, if the nonlinearity is pronounced, the standard $\sin^2\psi$ method cannot be used anymore and other special methods have to be used for the stress calculation (see Ref. Hauk, 1997).

When a multiphase material is investigated, all phases with an amount larger than 10% should be measured. In order to calculate macroscopic residual stresses in a

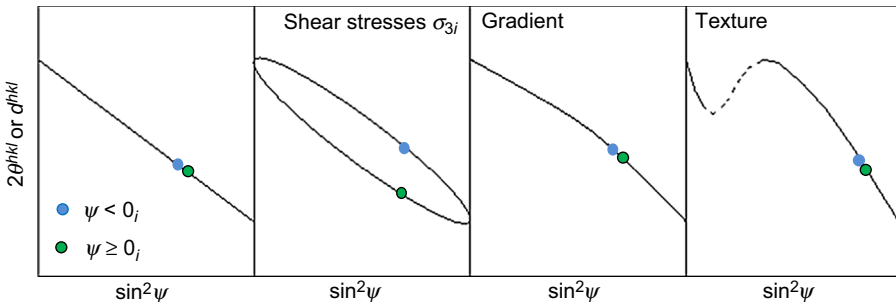


Figure 4.17 Different types of $\sin^2\psi$ distributions depending on the investigated material.

multiphase material, a weighted average of residual stresses in all phases can be calculated by Eq. [4.22], with σ_{ij}^l being the macrostresses along a given direction, f_i is the volume fraction of phase i , and σ_{ij}^i is the measured residual stress along a given direction in phase i (Fitzpatrick and Lodini, 2003). For this, the knowledge of the respective phase contents is required.

$$\sigma_{ij}^l = \sum f_i \times \sigma_{ij}^i \quad [4.22]$$

It has to be remarked that in multiphase materials, the stress component σ_{33} cannot always be considered to be zero (Behnken, 2003). Indeed, the macroscopic stress σ_{33} has to be zero at the surface, but different phases might exhibit σ_{33} residual stresses of the second kind with opposite signs if the microstructural periodicity is lower than the penetration depth of X-rays (Behnken, 2003). If a σ_{33} component is present, the slope of the $\sin^2\psi$ plot measured in a given direction is not only proportional to the normal stresses σ_{11} or σ_{22} anymore, but to $(\sigma_{11} - \sigma_{33})$ or $(\sigma_{22} - \sigma_{33})$. For the calculation of σ_{33} , very precise determination of the stress-free lattice spacing d_0 is then required (Hauk, 1997).

In order to perform residual stress measurements by XRD, several issues should be considered:

- The used diffractometer has to be aligned carefully and calibrated with known standards.
- Generally, positive and negative ψ from -45° to $+45^\circ$ in at least nine steps should be measured.
- Diffraction peaks without overlapping with other phases should be used.
- The measurement time should be long enough to measure well-defined peaks, and the measured 2θ range has to be large enough to measure the background at both sides of the peak.
- Diffractions peaks at high 2θ angles ($>100^\circ$) should be chosen for the measurements as errors due to misalignment of the diffractometer are strongly reduced.
- The sample preparation should not affect the residual stress state.
- This method is valid for monophase materials. If a multiphase material is investigated and the amount of secondary phases is significant ($>10\%$), measurements should be performed in all phases. Moreover, nonzero second kind residual stress components normal to the surface (σ_{33}) can be present in the different phases.
- When strong crystallographic texture or strong gradients are present, large errors can result.
- When the grain size is very large compared to the beam size, errors can result. In order to improve the results, sample oscillation should be used.
- If electrochemical layer removal is used, data correction should be used.
- Detailed information can be found in the norms (EN 15305:2008, 2008) and (ASTM E2860-12, 2012).

Examples of application

An example of a residual stress measurement performed at a turbine blade made of Ti6Al4V is presented. The measurement was performed with Nickel-filtered Cu-K α -Radiation in longitudinal direction at the root where a shot-peening treatment was applied. The measurements were performed in ω -mode due to accessibility

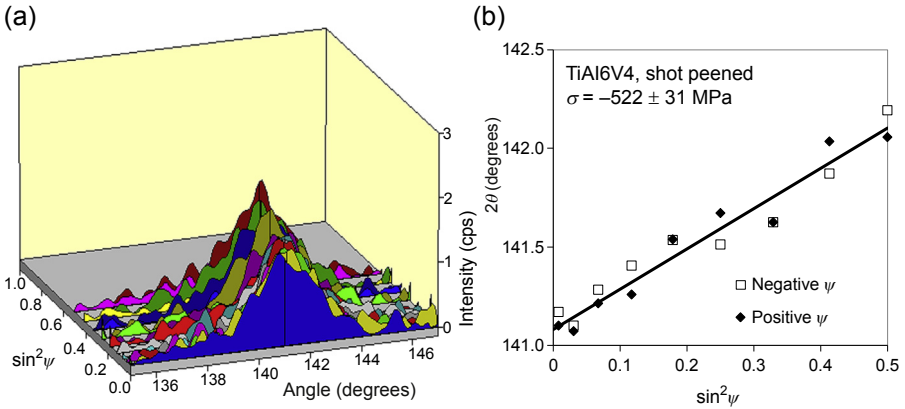


Figure 4.18 Residual stress measurement at a turbine-blade of TiAl6V4: (a) diffraction peaks for all ψ -angles; (b) $\sin^2\psi$ plot.

reason. The $\{213\}$ diffraction peak of α -Ti was measured with 19 different ψ -angles from -45° to $+45^\circ$. The measured diffraction peaks are shown in Fig. 4.18(a) for the different ψ -angles and the resulting $\sin^2\psi$ plot is given in Fig. 4.18(b). Slight scattering of the single peak positions can be observed, but no splitting or curved distribution is present. Therefore, the linear regression of the data set gives a reliable normal residual stress value of -522 ± 31 MPa.

A second example of XRD residual stress measurements concerns the investigation and the control of undesired distortion during the manufacturing of machine components like bearings. Cylindrical and tapered rings made from the steel-grade 100Cr6 were investigated after soft turning and subsequent heat treatment. As known from earlier investigations, the combined effect of clamping and machining can introduce inhomogeneous residual stresses around the periphery of the rings (Epp and Hirsch, 2010). XRD residual stress measurements were executed by Bragg–Brentano diffractometers (type F, Siemens AG, Germany) equipped with scintillation counters. The measurements were performed with vanadium-filtered Cr-K α -radiation with 35 kV and 35 mA and a primary beam diameter of 2.4 mm. The lattice planes $\{211\}$ were measured along 11 ψ angles from -45° to $+45^\circ$. The detector steps were 0.05° with a measurement time of 3 s/step. In order to have an almost complete surface characterization, residual stress measurements were done at 36 points in the middle height around the external periphery (every 10°) by automatic ring rotation, as shown in Fig. 4.19.

Due to different machining parameters (clamping tool and feed-rate), different distributions of residual stresses were measured around the outer circumference of the rings, as presented in Fig. 4.20(a) where a periodic distribution can be distinguished. Variation A and B were clamped with a 6-point clamping tool with respectively 0.1 and 0.4 mm feed-rate while the variations C and D were machined with the same respective feed-rates but with a clamping using a three jaw chuck. The inhomogeneous

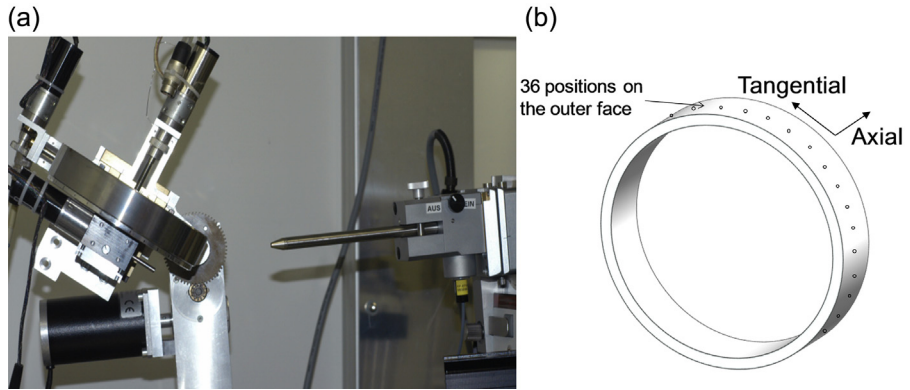


Figure 4.19 (a) Picture of the experimental set-up for automatic measurement of residual stresses around the circumference of a ring in axial direction; (b) sketch of a ring and positions measured by X-ray diffraction.

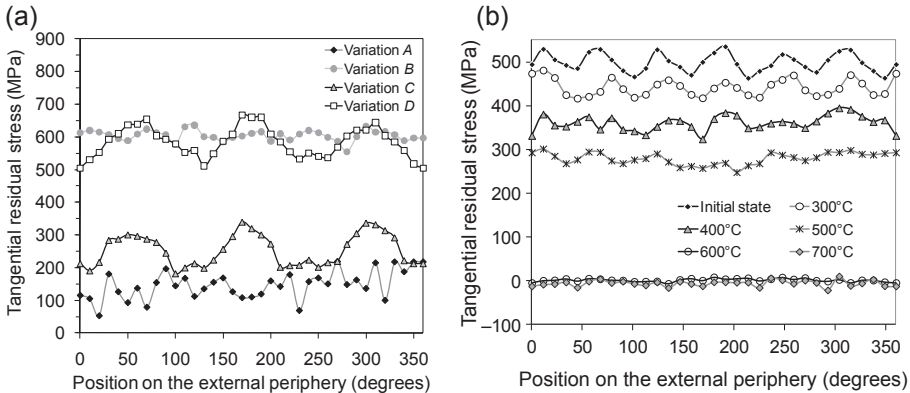


Figure 4.20 (a) Residual stress distribution for different machining parameters (Epp and Hirsch, 2010); (b) residual stress distribution measured at different rings after heating to different temperatures and cooling back to room temperature (Epp et al., 2011).

distribution is a distortion potential which can be released during subsequent heat treatment, leading to distortion. The thermally induced residual stress relaxation of a ring with an initial sixth order periodicity of the residual stress distribution is shown in Fig. 4.20(b), showing a progressive loss of periodicity and a general decrease of the residual stress level (Epp et al., 2011).

Finally, a last example of applications of XRD residual stress investigations concerns the effect of alternative peening methods on the fatigue properties of high-strength carburized steel gears. Indeed, it is well known that compressive residual stresses act like loading stresses and can therefore reduce the local loading

condition what is widely used to improve the fatigue properties of notched components. In order to take the effects of residual stresses on fatigue properties into account, the concept of local fatigue strength has been developed (Winderlich, 1990).

In the present case, the methods of water jet peening (WJP) and laser shock peening (LSP) are compared to shot peening (SP) as standard and as duo-process and investigated in terms of induced residual stresses and fatigue properties (Epp and Zoch, 2014). XRD measurements of residual stresses and retained austenite have been executed with a Bragg–Brentano diffractometer (type MZ VI E, GE Inspection Technologies) equipped with vanadium-filtered Cr-K α -radiation. The primary beam was focused to a diameter of 0.3 mm by a focusing polycapillary in order to measure in the notched area with a radius of curvature of 1.5 mm. As a consequence of the small beam size, an oscillating translation in notch direction was used in order to improve the grain statistic. A position sensitive detector recorded the diffracted beam of {211} lattice planes of martensite and {220} of retained austenite. Measurements were performed in χ -mode with 15 tilt-angles from -45° to $+41^\circ$ perpendicularly to the root. In order to establish depth profiles, measurements were conducted at different preselected depths after electropolishing. The electropolishing was carried out using an electrolyte solution containing 80% H₃PO₄ and 20% H₂SO₄. Correction of the effect of layer removal on the residual stress values in the depth was performed according to Moore and Evans (Totten et al., 2002).

SP leads to very high compressive residual stresses (up to -1650 MPa) with a maximal affected depth of about $170\text{ }\mu\text{m}$. After WJP, maximum residual stresses of about -1000 MPa with very low depth ($50\text{ }\mu\text{m}$) are present, while the LSP leads to very large affected depths ($<1\text{ mm}$) and residual stresses of about -1100 MPa (Fig. 4.21(a)). In terms of fatigue properties, the SP process shows the highest improvement compared to the heat treated state ($+47\%$) while the LSP and the WJP leads to an improvement of $+15\%$ and $+23\%$, respectively (Fig. 4.21(b)). These results showed that the depth of the compressive residual stresses does not play an important role on the improvement of the bending fatigue properties for the considered notched geometry

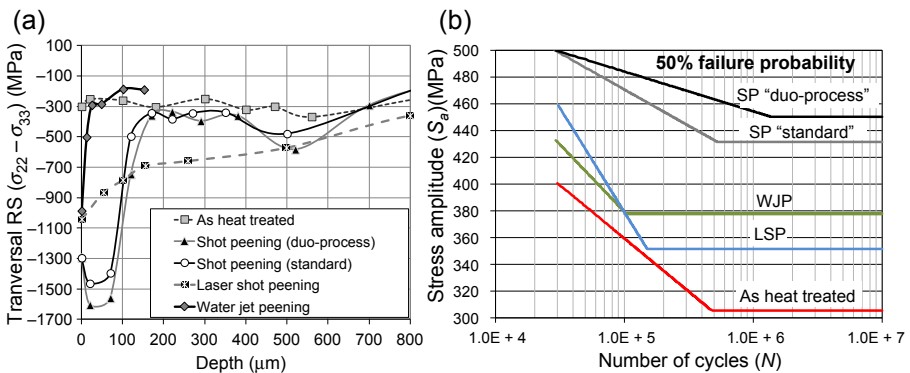


Figure 4.21 (a) Residual stress depth profiles measured for different surface peening treatments; (b) S–N curves obtained for different surface peening treatments (Epp and Zoch, 2014).

but that only the maximum compressive residual stress at the surface was the major factor (Epp and Zoch, 2014).

4.3.3 Texture measurements

In polycrystalline materials for engineering applications, several production steps are required to reach the final state with the desired properties. All the process steps, starting from material casting, to hot or cold forming processes, machining processes as well as heat treatment or joining operations can lead to the formation of a more or less strong crystallographic texture. This means that the present phases are not randomly oriented within the microstructure, but that they present a preferred orientation regarding their crystallographic structure. Depending on the structure of the considered phases and the process step responsible for the creation of the texture, different preferred orientations can be present. The knowledge about the presence of a crystallographic texture in a polycrystalline material can be of major importance. Indeed, it generally influences several macroscopic material properties due to the anisotropic properties of the crystal structure itself. If the orientation of the crystallites is not random, the macroscopic properties will therefore not be isotropic but will present variations in the different directions. Such properties are mechanical properties like elastic constants, magnetic properties, chemical properties, etc. Moreover, information about texture can be required for the reliable investigation of phase contents and residual stresses.

4.3.3.1 Texture measurements by X-ray diffraction

Due to the phase selective measurements and the possibility of precise sample orientation with the available equipment, XRD has been developed to become one of the major methods for the characterization of the crystallographic texture of materials. The method is based on the evaluation of the intensity variation of one or several diffraction peaks of a given phase along a large amount of sample orientation. For this, the sample is typically placed in a four-circle diffractometer with eulerian cradle (Fig. 4.7), and a defined 2θ range covering one diffraction peak is recorded in a similar manner as it would be the case in residual stress measurements. However, not the position of the diffraction peak is of interest but the peak intensity, as the intensity recorded in a given direction is directly proportional to the volume fraction of crystallites in diffracting condition in this direction. Measurements in transmission mode can be performed, but for solid samples, most applications use the reflexion mode. In texture analysis in reflexion mode, the previously defined angles are redefined as: $\omega = \theta$; $\chi = \alpha$; and $\varphi = \beta$.

The base of XRD texture analysis is the measurement of pole figures. For this, the same coordinate system as presented in Fig. 4.13 is applied. A combination of φ - and ψ -angles is used to measure the considered diffraction peak and its intensity variation. As a list of all measured intensities would be difficult to interpret, a graphical representation allows the evaluation of the results. With the help of a stereographic projection (Fig. 4.22), the intensity variation for the investigated φ - and ψ -angles can be

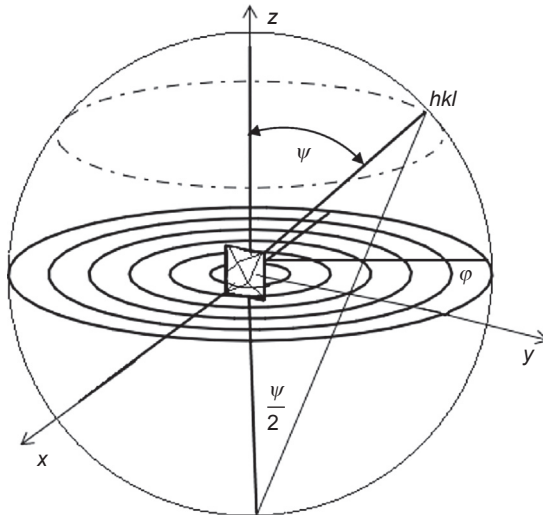


Figure 4.22 Principle of a stereographic projection for the determination of pole figures.

represented for all combination of these angles. For each considered lattice plans (hkl), an own pole figure can be measured.

For the measurement of pole figures by XRD, different strategies can be used. Generally, combinations of α - and β -angles in small discrete steps of several degrees are used with a complete rotation of the sample ($0 < \beta < 360^\circ$) and maximum tilt angles (α) of 70° – 80° . This limitation is due to the fact that at a higher angle, the grazing incidence of the X-ray beam leads to a very elongated beam size on the sample. High absorption and defocusing effects can then occur leading to decreasing reliability of the values. In general, absorption and defocusing effects should be corrected by using a reference sample without texture (powder) in order to compensate intensity variations occurring at large tilt angles. Other measurement strategies using, for example, ϕ - and ψ -continuous scanning can be used (Spieß et al., 2009). Due to the large number of sample orientations that have to be evaluated, the measurement of a single pole figure can take up to several days. Therefore, position sensitive detectors or 2-D detectors are particularly indicated for texture analysis. According to the crystal symmetry and the sample symmetry (due to the process step responsible for the created texture), varying ranges of the pole figure have to be measured in order to obtain representative texture measurement (Spieß et al., 2009).

One major field of application of texture measurements is the analysis of cold-rolled metal sheets, which has already been used for several decades. For example, online (in-process) texture analysis methods were already developed and implemented in the 1980s in the production line at Hoesch Stahl AG in Dortmund, Germany (Kopineck and Otten, 1987). The technique was based on energy-dispersive measurements in transmission mode using the continuous spectrum of a tungsten-anode to measure portions of several pole figures. For this, two detectors were used, allowing them to measure

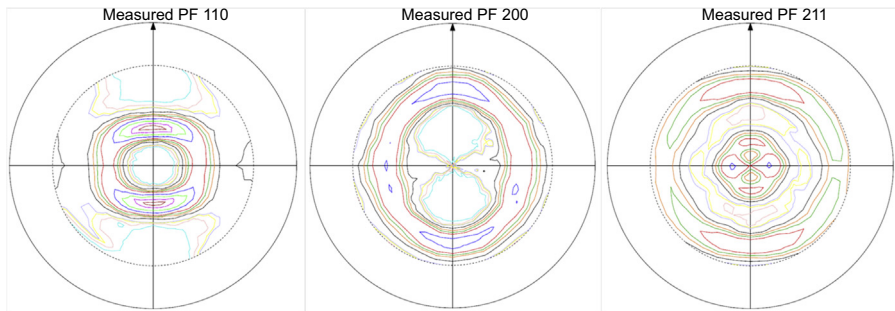


Figure 4.23 Pole figures measured at a cold-rolled α -Fe thin sheet.

simultaneously at two β -angles. In preliminary investigations, it had been demonstrated that the intensity of Fe- α -{211} and Fe- α -{220} peaks are directly correlated to the plastic strain ratio (Lankford coefficient, or R -value) of the sheets, and this ratio is an indicator of formability of recrystallized low-carbon steel as in deep-drawing processes. These texture measurements therefore allowed an online quality control of the steel-sheet production.

An illustration of typical pole figure measurements is presented in Fig. 4.23 showing the {110}, {200}, and {211} pole figures measured in the core at a cold-rolled thin sheet of armco-Iron (α -Fe) with of 100 μm thickness. Angle-dispersive measurements were carried out on an ETA 3003 (GE Inspection Technology, Ahrensburg, Germany) with Cr- $k\alpha$ radiation anode with a current of 40 mA and a voltage of 40 kV. The beam was collimated to a diameter (\varnothing) of 2 mm and the diffracted signal was measured by using a position sensitive detector with an angular range of $10^\circ 2\theta$ and a resolution of 0.1° within 21 s for each α and β combination. The diffraction peaks were recorded from 0° to 70° with an angular spacing of 5° in α and from 0° to 350° with an angular spacing of 10° in β . The total time for measuring these three pole figures was 35 h.

Iso-intensity lines are represented, indicating the zones of intensity concentration. For the three pole figures, different zones with high intensity can be observed. The symmetry of the pole figures shows that the measurement of a β -range of 0° – 90° would have been sufficient to describe the texture.

4.3.3.2 Evaluation of texture measurements

Based on measured pole figures, a quantitative analysis of the crystallographic can be performed by using the orientation distribution function (ODF) (Bunge, 1982). The ODF, $f(g)$ gives the volume fraction of crystallites $dV(g)$ which are contained within the range dg of the crystallographic orientation g regarding a defined coordinate system measured within the considered Volume V (Eq. [4.23]). The ODF is scaled to 1 over all sample's orientations (Eq. [4.24]) (Bunge, 1982). It has to be remarked that the determination of the ODF requires the measurement of several pole figures. The higher the crystal symmetry, the less pole figures are needed.

$$f(g)dg = \frac{dV(g)}{V} \quad [4.23]$$

$$\int_g f(g)dg = 1 \quad [4.24]$$

In order to describe ODFs, Euler's angles are widely used, which consists of a system of three consecutive rotations. First, the crystal coordinate system should be oriented in such a manner that the axes are parallel to those of the sample coordinate system. Then, the crystal coordinate system is rotated about the Z' -axis through the angle φ_1 . Second, the X' -axis (in its new orientation) is rotated through the angle Φ . Finally, a third rotation around the new axis Z' by the angle φ_2 is following. Any crystallite orientation g can be described by these three angles (Bunge, 1982).

The ODF has to be calculated on the basis of the measured pole figures. For this, different methods can be used: the direct method, the independent component analysis, and the series expansion method which is the most widely used method (Spieß et al., 2009).

In the series expansion method, the ODF is calculated via a series of generalized spherical harmonic functions $T_\lambda^{mn}(g)$ as given in Eq. [4.25]. The $T_\lambda^{mn}(g)$ are known functions and can be calculated for all orientations g , while the unknown series expansion coefficients C_λ^{mn} can then be determined (Bunge, 1982).

$$f(g) = \sum_{\lambda=0}^{\lambda_{\max}} \sum_{m=-\lambda}^{+\lambda} \sum_{n=-\lambda}^{+\lambda} C_\lambda^{mn} T_\lambda^{mn}(g) \quad [4.25]$$

As already reported previously, the plastic strain ratio (R -value) of metal sheets was identified to be directly related to diffraction peak intensity. A deeper correlation is possible by the use of fourth order series expansions coefficient of the ODF (Banabic et al., 2000). Indeed, during cold-rolling of cubic materials an orthorhombic texture is generated. The lowest-order nonrandom approximation is then the fourth order ($\lambda = 4$) that describes the influence of a texture on the elastic properties of the material by the knowledge of the three fourth order series expansion coefficients C_4^{1x} . This can be used for the evaluation of the R -values in sheet material (Banabic et al., 2000).

From the ODF, a convenient manner to describe and compare the sharpness of a texture of different samples is to calculate the texture index J (Eq. [4.26]), which can be calculated from the coefficients of the series expansion. The index can be between 1 for a texture-free sample and infinite for a single crystal (Bunge, 1982).

$$J = \int_g [f(g)]^2 dg \quad [4.26]$$

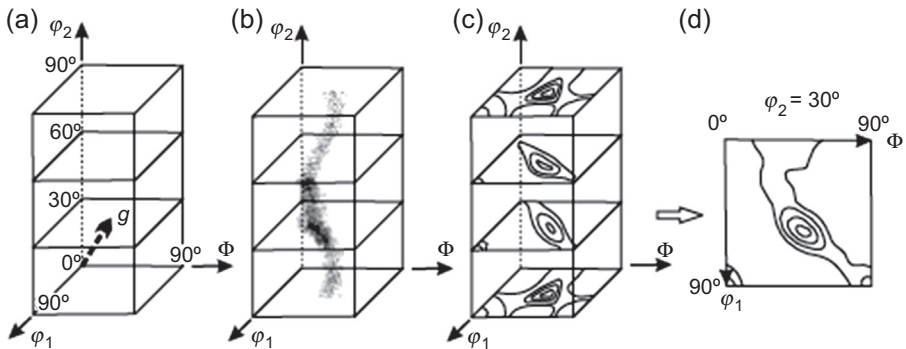


Figure 4.24 Representation of ODFs in Euler space: (a) Euler space; (b) scatter-plot of the 3-D ODF representation; (c) 3-D ODF representation as a succession of 2-D projections; and (d) Example of a 2D-projection at constant ϕ_2 (Spieß et al., 2009).

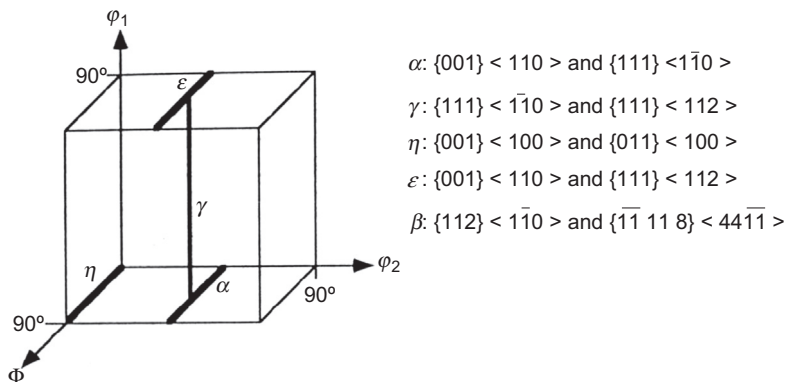


Figure 4.25 Ideal fiber-texture components of rolled body-centered-cubic metals (Spieß et al., 2009).

The ODF can be visualized as 3-D representation of iso-intensity surface in the Euler space or as a succession of 2-D projections of iso-intensity lines at different positions in the Euler space. The different possibilities of ODF representation are illustrated in Fig. 4.24.

According to the crystal structure of the investigated phase, different typical textures can be observed by using the representation in the Euler space. As an example, the ideal fiber components for rolled body-centered-cubic (BCC) metals are presented in Fig. 4.25.

The ODF calculated by means of series expansion from the three pole figures measured at a cold-rolled α -Fe thin sheet presented in Fig. 4.23 is shown as 3-D representation in Fig. 4.26 and as 2-D projections of ϕ_1 in Fig. 4.27. Compared

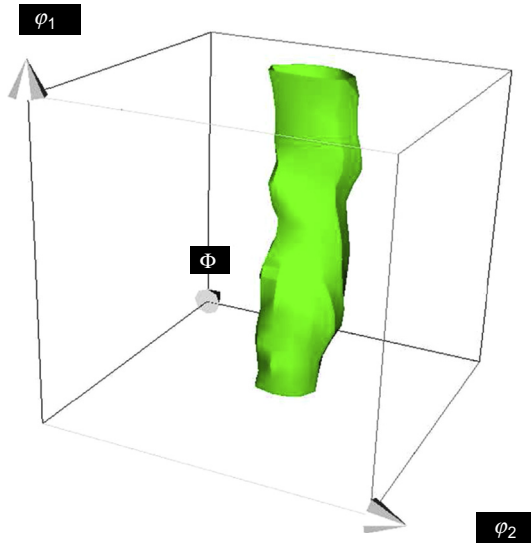


Figure 4.26 3-D representation of the orientation distribution function of a cold-rolled α -Fe thin sheet.

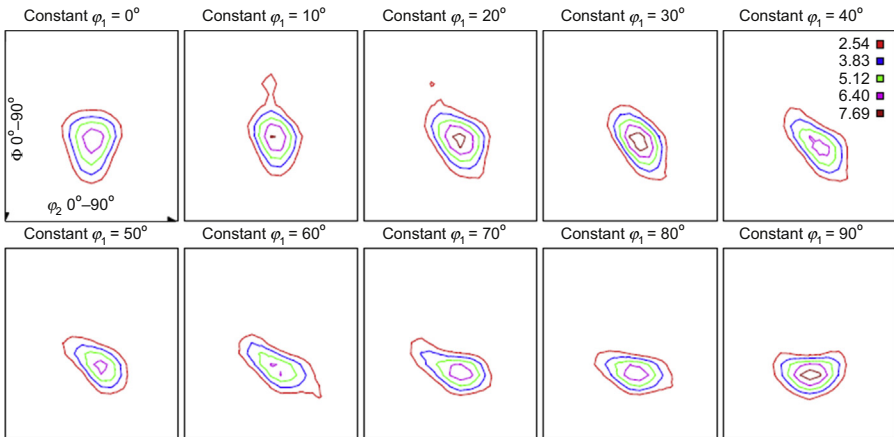


Figure 4.27 Orientation distribution function of a cold-rolled α -Fe thin sheet represented as 2-D projections at ϕ_1 between 0° and 90° .

to the known texture components in BCC metals given in Fig. 4.25, it can be observed that an almost ideal γ -fiber is present, as expected for cold-rolled BCC materials.

Finally, another common method for the representation of crystallographic texture is the so-called inverse pole figure. The inverse pole figure is a sort of opposite to the pole figure and it shows how a defined direction in the sample coordinate system is distributed in the crystal coordinate system (Bunge, 1982).

4.3.4 *In situ* X-ray diffraction experiments during quenching of a steel ball bearing

One recent example of an application of in situ XRD experiments is the investigation of martensitic transformation during rapid quenching of ball-bearing steel using the angle-dispersive method with synchrotron radiation (Epp, 2014). The experiments were performed at european synchrotron radiation facility (ESRF) on Beamline ID11 in transmission mode with a monochromatic beam (energy of 71 keV) and varying heat treatment parameters. By variations of the austenitizing temperature, different carbon contents in solution were set in hypereutectoid steel, leading to different behavior during quenching. The temperature was controlled by the use of a type-K thermocouple welded on the surface of the samples.

After austenitizing at different temperatures, increasing amount of carbon is in solid solution in the austenite leading to a decreasing martensite start temperature and a modified transformation kinetic. With a measuring frequency of 1 Hz, complete diffraction

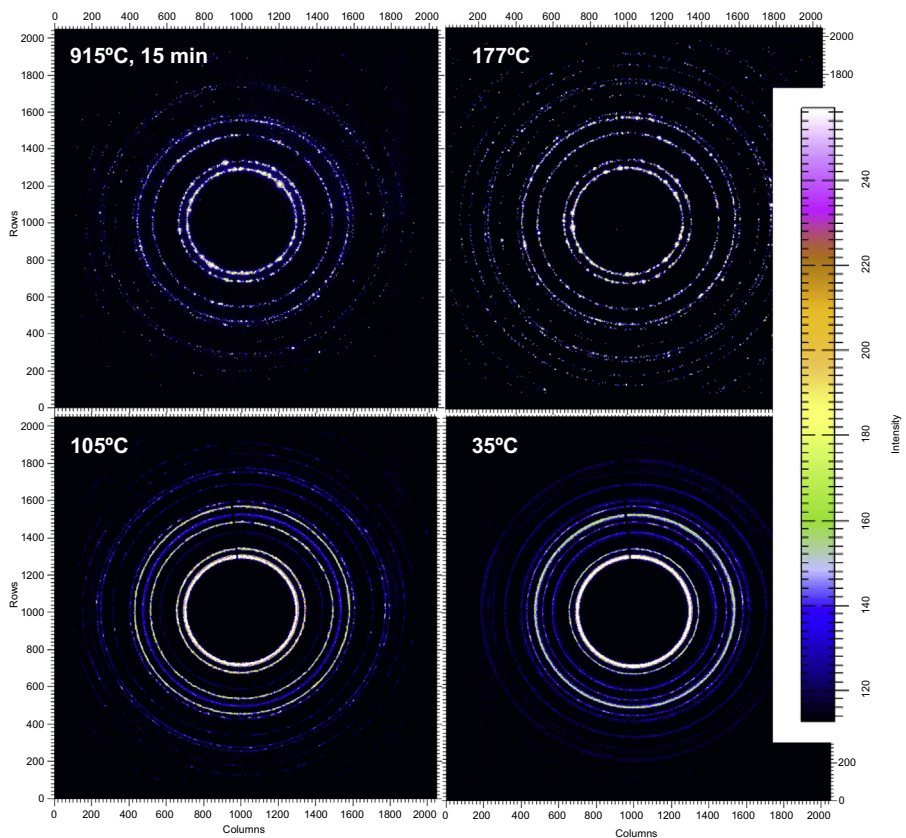


Figure 4.28 2-D diffraction frames taken at different temperatures during quenching (Epp, 2014).

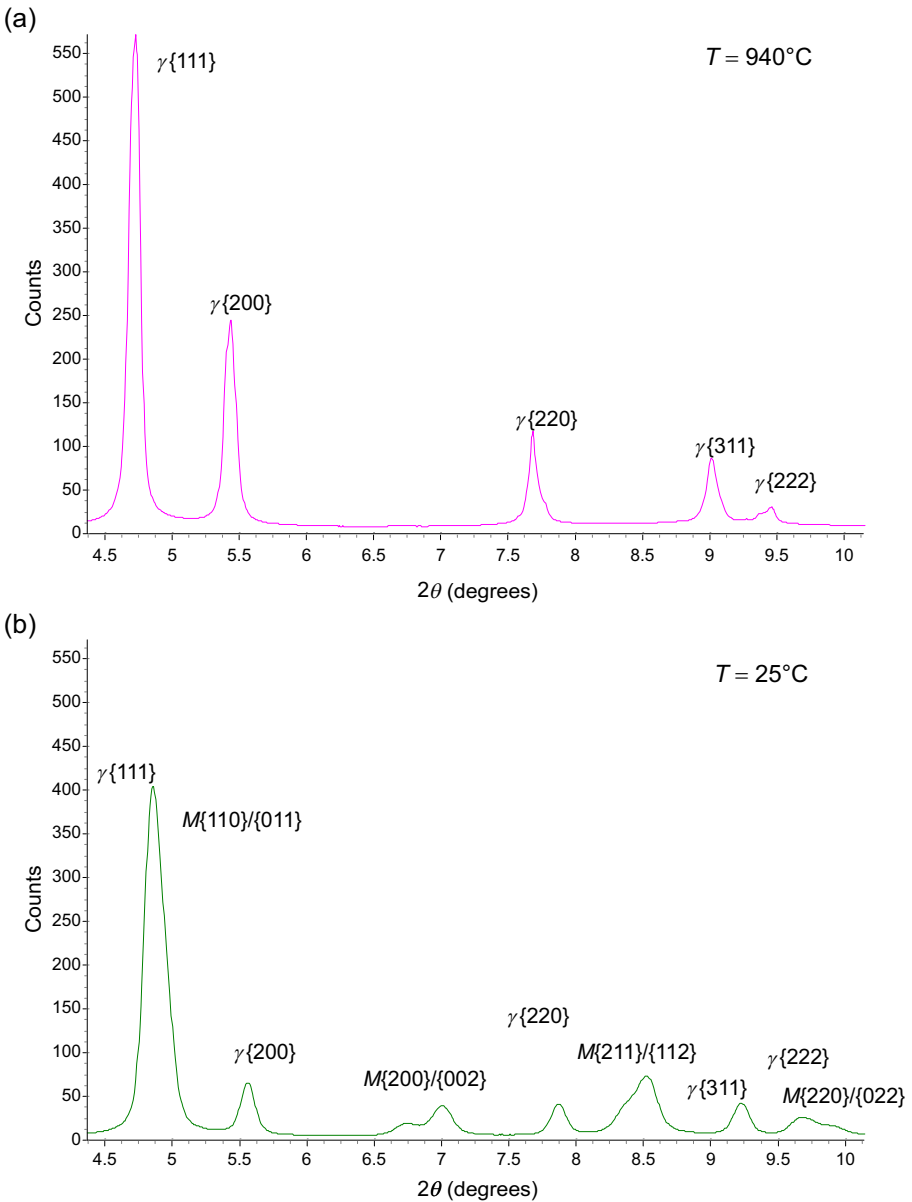


Figure 4.29 Integrated diffraction patterns (a) taken at austenitizing temperature and (b) after quenching.

rings were measured (Fig. 4.28) and after integration to obtain classic diffraction patterns, Rietveld refinement could be used to perform phase analyses. Fig. 4.29 shows two integrated diffraction patterns at austenitizing temperature (a) and after quenching to room temperature (b), showing the good signal quality allowing precise quantitative

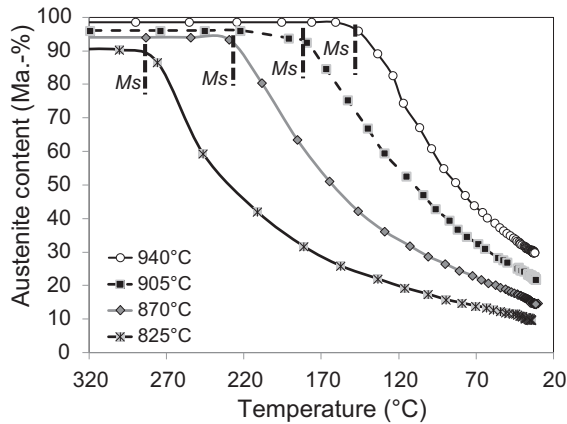


Figure 4.30 Evolution of austenite content during quenching of four samples after austenitizing at different temperatures (Epp, 2014).

analyses. By using Rietveld refinements, the temperature-dependent phase contents could be determined and the transformation kinetics could be described (Fig. 4.30) (Epp, 2014). Further, time- and temperature-resolved evolution of stresses and phase specific density could be characterized (Epp, 2014).

4.4 Conclusions and future trends

Since the discovery of X-rays and the first experiments on XRD by crystals, XRD methods have become very powerful state of the art techniques for advanced material characterization. In the last decades, developments in computer technologies, microelectronics, and data analysis have allowed to make these techniques broadly available and convenient to apply. As a consequence, the knowledge about crystal structure, microstructure, and properties of components could have been strongly improved, allowing the design of high performance materials and components.

On one side, hardware developments (like X-ray source, optics, or detectors) leading to increasing precisions and decreasing measurement time enables increasingly effective and reliable investigations. One innovation in this field is the liquid-metal X-ray source, allowing to reach high beam intensity as the heat development is strongly reduced.

On the other side, new developments of the presented methods are still ongoing, especially for complex materials, geometries, and applications. For example, the advancements of the energy-dispersive methods or high resolution XRD are opening new possibilities of investigations.

Further, the analyses under nonambient conditions or of transient processes by in situ or in-process measurements with XRD methods have an enormous potential for further improvement of materials and manufacturing processes.

Finally, the accessibility of synchrotron-based XRD methods pushes the limits of material characterization concerning the spatial resolution (down to the nanometer-sized beam), but also with very high beam intensity, allowing measuring with high frequencies of up to 30 Hz or more.

References

- ASTM E2860-12, 2012. Standard Test Method for Residual Stress Measurement by X-Ray Diffraction for Bearing Steels.
- ASTM, October 2000. Standard Practice for X-Ray Determination of Retained Austenite in Steel with Near Random Crystallographic Orientation. Designation: E975–13.
- Babu, S.S., Specht, E.D., David, S.A., Karapetrova, E., Zschack, P., Peet, M., et al., 2007. Time-resolved X-ray diffraction investigation of austenite and transformation to bainite. In: Proceedings of the First International Symposium on Steel Science.
- Banabic, D., Bünge, H.J., Pöhlant, K., Tekkaya, A.E., 2000. Formability of metallic materials. In: Banabic, D. (Ed.), Plastic Anisotropy, Formability Testing and Forming Limits. Springer Verlag, Heidelberg.
- Behnken, H., 2003. Mikrospannungen in vielkristallinen und heterogenen Werkstoffen. Shaker Verlag, Aachen.
- Bragg, W.L., 1913. The diffraction of short electromagnetic waves by a crystal. *Proc Camb Philos Soc* 17, 43–57.
- Bruker-AXS, 2008. TOPAS V4: General Profile and Structure Analysis Software for Powder Diffraction Data. User's manual. Bruker-AXS, Karlsruhe (Germany).
- Bunge, H.J., 1982. Texture Analysis in Materials Science. Butterworths, London.
- Curfs, C., 2002. Time-Resolved Studies of the Self-Propagating High-Temperature Synthesis of Compounds from the System Aluminium-Nickel-Titanium-Carbon [Ph.D. Thesis]. Université Joseph Fourier, Grenoble (France).
- Dinnebier, R.E., Billinge, S.J.L., 2008. Powder Diffraction, Theory and Practice. The Royal Society of Chemistry.
- Eigenmann, B., Macherauch, E., 1995. Röntgenographische Untersuchung von Spannungszuständen in Werkstoffen- Teil II. *Mater Werkst* 3, 148–160.
- Elmer, J.W., Wong, J., Fröba, M., Waide, P.A., Larson, E.M., 1996. Analysis of heat-affected zone phase transformations using in situ spatially resolved X-ray diffraction with synchrotron radiation. *Metall Mater Trans A* 27A, 775–782.
- EN 15305:2008, 2008. Non-Destructive Testing - Test Method for Residual Stress Analysis by X-Ray Diffraction.
- Epp, J., Hirsch, T., 2010. Residual stress state characterization of machined components by X-ray diffraction and multiparameter micromagnetic methods. *Exp Mech* 50-1, 195–204.
- Epp, J., Surm, H., Kessler, O., Hirsch, T., 2007. In situ X-ray phase analysis and computer simulation of carbide dissolution of ball bearing steel at different austenitizing temperatures. *Acta Mater* 55-17, 5959–5967.
- Epp, J., Surm, H., Hirsch, T., Hoffmann, F., 2011. Residual stress relaxation during heating of bearing rings produced in two different manufacturing chains. *J Mater Process Technol* 211, 637–643.
- Epp, J., Zoch, H.-W., 2014. Comparison of water jet peening and laser shock peening with shot peening for the improvement of fatigue properties of case hardened steel gears. In:

- Wagner, L. (Ed.), Proceedings of the Twelfth International Conference on Shot Peening, September 15–18, 2014, Goslar, Germany, pp. S214–S219.
- Epp, J., 2014. Investigation of triaxial stress state in retained austenite during quenching of a low alloy steel by in situ X-ray diffraction. *Adv Mater Res* 996, 525–531.
- Fitzpatrick, M.E., Lodini, A., 2003. Analysis of Residual Stress by Diffraction Using Neutron and Synchrotron Radiation. Taylor and Francis, London.
- Friedrich, W., Knipping, P., von Laue, M., 1913. Interferenzerscheinungen bei Röntgenstrahlen. *Ann Phys* 41, 971–990.
- Günther, D., 2004. Einfluss unterschiedlicher Chromgehalte auf die Ausbildung von Eigenspannungen und Phasenzusammensetzung beim Gasnitrieren von Stählen [Ph.D. thesis]. University of Bremen.
- Guinebretière, R., 2006. Diffraction Des Rayons X Sur Échantillons Polycristallins, second ed. Lavoisier, Paris.
- Hölzer, G., Fritsch, M., Deutsch, J., Härtwig, M., Förster, E., 1997. $K_{\alpha 1,2}$ and $K_{\beta 1,3}$ X-ray emission lines of the 3d transition metals. *Phys Rev A* 56, 4554–4568.
- Hauk, V., 1997. Structural and Residual Stress Analysis by Nondestructive Methods. Elsevier Science, Amsterdam.
- He, B.B., Preckwinkel, U., Smith, K.L., 2000. Fundamentals of two-dimensional X-ray diffraction. *Adv X-ray Anal* 43, 273–280.
- Kern, A., Coelho, A.A., Cheary, R.W., 2004. Convolution based profile fitting. In: Mittemeijer, E., Scardi, P. (Eds.), Diffraction Analysis of the Microstructure of Materials, Springer Series in Materials Science, vol. 68, pp. 17–50.
- Klug, H.P., Alexander, L.E., 1974. X-Ray Diffraction Procedures for Polycrystalline and Amorphous Materials, second ed. John Wiley & Sons, New York-Sydney-Toronto.
- Kopineck, H.-J., Otten, H., 1987. Texture analyzer for on-line rm-value estimation. *Textures Microstruct* 7, 97–113.
- Kostov, V., Gibmeier, J., Wilde, F., Staron, P., Rössler, R., Wanner, A., 2012. Fast in-situ phase and stress analysis during laser surface treatment: a synchrotron X-ray diffraction approach. *Rev Sci Instrum* 83, 1–11.
- Kromm, A., Kannengiesser, T., Gibmeier, J., 2010. In situ observation of phase transformations during welding of low transformation temperature filler material. *Mater Sci Forum* 638–642, 3769–3774.
- Kruijver, S., Zhao, L., Sietsma, J., Offerman, E., van Dijk, N., Margulies, L., et al., 2002. In situ observations on the austenite stability in TRIP-steel during tensile testing. *Steel Res* 73 (6/7), 236–241.
- Macherauch, E., Wohlfahrt, H., Wolfstieg, U., 1973. Zur zweckmäßigen Definition von Eigenspannungen. *Härterei-Technische Mitt* 28-3, 201–211.
- Macherauch, E., Zoch, H.-W., 2014. Röntgenografische Eigenspannungsbestimmung in Praktikum in Werkstoffkunde, 12th ed. Springer.
- Noyan, I.C., Cohen, J.B., 1987. Residual stress, measurement by diffraction and interpretation. Springer Verlag.
- Prevey, P.S., 1986. X-ray diffraction residual stress techniques. In: Metals Handbook, 10 Metal Parks. ASM, pp. 380–392.
- Prince, E., 2004. Volume C - Mathematical, Physical and Chemical Tables, International Tables for Crystallography, third ed. Kluwer Acad. Publ., Dordrecht.
- Recke, S., Hirsch, T., 2007. Röntgenographische In-situ-Messungen der Eigenspannungen zwischen 750°C und 900°C. Optimierung der Messeinrichtung. *MP Mater Test* 10, 509–514.
- Rocha, A., da, S., Hirsch, T., 2005. Fast in situ X-ray diffraction phase and stress analysis during complete heat treatment cycles of steel. *Mater Sci Eng A* 395, 195–207.

- Roentgen, W.C., 1895. Über eine neue Art von Strahlen. In: Sitzungsbericht der Würzburg Physik und Medicin Gesellschaft.
- Schwartz, L.H., Cohen, J.B., 1987. Diffraction from Materials. Springer Verlag, Berlin.
- Spieß, L., Teichert, G., Schwarzer, R., Behnken, H., Genzel, C., 2009. Moderne Röntgenbeugung, second ed. Teubner Verlag, Wiesbaden.
- Tomala, V., 1998. In-situ Eigenspannungsmessungen bei hohen Temperaturen in CVD-beschichteten Stahlsubstrat-Verbundwerkstoffen [Ph.D. thesis]. University of Bremen.
- Totten, G., Howes, M., Inoue, T. (Eds.), 2002. Handbook of Residual Stress and Deformation of Steel. ASM International.
- Will, G., 2006. Powder Diffraction: The Rietveld Method and The Two Stage Method. Springer Verlag.
- Winderlich, B., 1990. Das Konzept der lokalen Dauerfestigkeit und seine Anwendung auf martensitische Randschichten, insbesondere Laserhärtungsschichten. Mat.-wiss U Werkst 21, 378–389.

Further reading

- Bunge, H.J., 1982. Texture Analysis in Materials Science. Butterworths, London.
- Dinnebier, R.E., Billinge, S.J.L., 2008. Powder Diffraction, Theory and Practice. The Royal Society of Chemistry.
- Hauk, V., 1997. Structural and Residual Stress Analysis by Nondestructive Methods. Elsevier Science, Amsterdam.
- Noyan, I.C., Cohen, J.B., 1987. Residual Stress, Measurement by Diffraction And Interpretation. Springer Verlag.
- Spieß, L., Teichert, G., Schwarzer, R., Behnken, H., Genzel, C., 2009. Moderne Röntgenbeugung, second ed. Teubner Verlag, Wiesbaden.